PHYSICAL REVIEW C **86**, 054908 (2012)

Inclusive charged hadron elliptic flow in Au + Au collisions at $\sqrt{s_{NN}} = 7.7$–39 GeV

L. Adamczyk,[1] G. Agakishiev,[21] M. M. Aggarwal,[34] Z. Ahammed,[52] A. V. Alakhverdyants,[21] I. Alekseev,[19] J. Alford,[22] B. D. Anderson,[22] C. D. Anson,[31] D. Arkhipkin,[4] E. Aschenauer,[4] G. S. Averichev,[21] J. Balewski,[26] A. Banerjee,[52] Z. Barnovska,[14] D. R. Beavis,[4] R. Bellwied,[48] M. J. Betancourt,[26] R. R. Betts,[10] A. Bhasin,[20] A. K. Bhati,[34] H. Bichsel,[54] J. Bielcik,[13] J. Bielcikova,[14] L. C. Bland,[4] I. G. Bordyuzhin,[19] W. Borowski,[45] J. Bouchet,[22] A. V. Brandin,[29] S. G. Brovko,[6] E. Bruna,[56] S. Bültmann,[32] I. Bunzarov,[21] T. P. Burton,[4] J. Butterworth,[40] X. Z. Cai,[44] H. Caines,[56] M. Calderón de la Barca Sánchez,[6] D. Cebra,[6] R. Cendejas,[7] M. C. Cervantes,[46] P. Chaloupka,[14] Z. Chang,[46] S. Chattopadhyay,[52] H. F. Chen,[42] J. H. Chen,[44] J. Y. Chen,[9] L. Chen,[9] J. Cheng,[49] M. Cherney,[12] A. Chikanian,[56] W. Christie,[4] P. Chung,[14] J. Chwastowski,[11] M. J. M. Codrington,[46] R. Corliss,[26] J. G. Cramer,[54] H. J. Crawford,[5] X. Cui,[42] A. Davila Leyva,[47] L. C. De Silva,[48] R. R. Debbe,[4] T. G. Dedovich,[21] J. Deng,[43] R. Derradi de Souza,[8] S. Dhamija,[18] L. Didenko,[4] F. Ding,[6] A. Dion,[4] P. Djawotho,[46] X. Dong,[25] J. L. Drachenberg,[46] J. E. Draper,[6] C. M. Du,[24] L. E. Dunkelberger,[7] J. C. Dunlop,[4] L. G. Efimov,[21] M. Elnimr,[55] J. Engelage,[5] G. Eppley,[40] L. Eun,[25] O. Evdokimov,[10] R. Fatemi,[23] S. Fazio,[4] J. Fedorisin,[21] R. G. Fersch,[23] P. Filip,[21] E. Finch,[56] Y. Fisyak,[4] C. A. Gagliardi,[46] D. R. Gangadharan,[31] F. Geurts,[40] A. Gibson,[51] S. Gliske,[2] Y. N. Gorbunov,[12] O. G. Grebenyuk,[25] D. Grosnick,[51] S. Gupta,[20] W. Guryn,[4] B. Haag,[6] O. Hajkova,[13] A. Hamed,[46] L-X. Han,[44] J. W. Harris,[56] J. P. Hays-Wehle,[26] S. Heppelmann,[35] A. Hirsch,[37] G. W. Hoffmann,[47] D. J. Hofman,[10] S. Horvat,[56] B. Huang,[4] H. Z. Huang,[7] P. Huck,[9] T. J. Humanic,[31] L. Huo,[46] G. Igo,[7] W. W. Jacobs,[18] C. Jena,[16] J. Joseph,[22] E. G. Judd,[5] S. Kabana,[45] K. Kang,[49] J. Kapitan,[14] K. Kauder,[10] H. W. Ke,[9] D. Keane,[22] A. Kechechyan,[21] A. Kesich,[6] D. Kettler,[54] D. P. Kikola,[37] J. Kiryluk,[25] I. Kisel,[25] A. Kisiel,[53] V. Kizka,[21] S. R. Klein,[25] D. D. Koetke,[51] T. Kollegger,[15] J. Konzer,[37] I. Koralt,[32] L. Koroleva,[19] W. Korsch,[23] L. Kotchenda,[29] P. Kravtsov,[29] K. Krueger,[2] I. Kulakov,[25] L. Kumar,[22] M. A. C. Lamont,[4] J. M. Landgraf,[4] S. LaPointe,[55] J. Lauret,[4] A. Lebedev,[4] R. Lednicky,[21] J. H. Lee,[4] W. Leight,[26] M. J. LeVine,[4] C. Li,[42] L. Li,[47] W. Li,[44] X. Li,[37] X. Li,[43] Y. Li,[49] Z. M. Li,[9] L. M. Lima,[41] M. A. Lisa,[31] F. Liu,[9] T. Ljubicic,[4] W. J. Llope,[40] R. S. Longacre,[4] Y. Lu,[42] X. Luo,[9] A. Luszczak,[11] G. L. Ma,[44] Y. G. Ma,[44] D. M. M. D. Madagodagettige Don,[12] D. P. Mahapatra,[16] R. Majka,[56] O. I. Mall,[6] S. Margetis,[22] C. Markert,[47] H. Masui,[25] H. S. Matis,[25] D. McDonald,[40] T. S. McShane,[12] S. Mioduszewski,[46] M. K. Mitrovski,[4] Y. Mohammed,[46] B. Mohanty,[30] M. M. Mondal,[46] B. Morozov,[19] M. G. Munhoz,[41] M. K. Mustafa,[37] M. Naglis,[25] B. K. Nandi,[17] Md. Nasim,[52] T. K. Nayak,[52] J. M. Nelson,[3] L. V. Nogach,[36] J. Novak,[28] G. Odyniec,[25] A. Ogawa,[4] K. Oh,[38] A. Ohlson,[56] V. Okorokov,[29] E. W. Oldag,[47] R. A. N. Oliveira,[41] D. Olson,[25] P. Ostrowski,[53] M. Pachr,[13] B. S. Page,[18] S. K. Pal,[52] Y. X. Pan,[7] Y. Pandit,[22] Y. Panebratsev,[21] T. Pawlak,[53] B. Pawlik,[33] H. Pei,[10] C. Perkins,[5] W. Peryt,[53] P. Pile,[4] M. Planinic,[57] J. Pluta,[53] D. Plyku,[32] N. Poljak,[57] J. Porter,[25] A. M. Poskanzer,[25] C. B. Powell,[25] D. Prindle,[54] C. Pruneau,[55] N. K. Pruthi,[34] M. Przybycien,[1] P. R. Pujahari,[17] J. Putschke,[55] H. Qiu,[25] R. Raniwala,[39] S. Raniwala,[39] R. L. Ray,[47] R. Redwine,[26] R. Reed,[6] C. K. Riley,[56] H. G. Ritter,[25] J. B. Roberts,[40] O. V. Rogachevskiy,[21] J. L. Romero,[6] J. F. Ross,[12] L. Ruan,[4] J. Rusnak,[14] N. R. Sahoo,[52] I. Sakrejda,[25] S. Salur,[25] A. Sandacz,[53] J. Sandweiss,[56] E. Sangaline,[6] A. Sarkar,[17] J. Schambach,[47] R. P. Scharenberg,[37] A. M. Schmah,[25] B. Schmidke,[4] N. Schmitz,[27] T. R. Schuster,[15] J. Seele,[26] J. Seger,[12] P. Seyboth,[27] N. Shah,[7] E. Shahaliev,[21] M. Shao,[42] B. Sharma,[34] M. Sharma,[55] S. S. Shi,[9] Q. Y. Shou,[44] E. P. Sichtermann,[25] R. N. Singaraju,[52] M. J. Skoby,[18] D. Smirnov,[4] N. Smirnov,[56] D. Solanki,[39] P. Sorensen,[4] U. G. deSouza,[41] H. M. Spinka,[2] B. Srivastava,[37] T. D. S. Stanislaus,[51] S. G. Steadman,[26] G. S. F. Stephans,[26] J. R. Stevens,[18] R. Stock,[15] M. Strikhanov,[29] B. Stringfellow,[37] A. A. P. Suaide,[41] M. C. Suarez,[10] M. Sumbera,[14] X. M. Sun,[25] Y. Sun,[42] Z. Sun,[24] B. Surrow,[26] D. N. Svirida,[19] T. J. M. Symons,[25] A. Szanto de Toledo,[41] J. Takahashi,[8] A. H. Tang,[4] Z. Tang,[42] L. H. Tarini,[55] T. Tarnowsky,[28] D. Thein,[47] J. H. Thomas,[25] J. Tian,[44] A. R. Timmins,[48] D. Tlusty,[14] M. Tokarev,[21] S. Trentalange,[7] R. E. Tribble,[46] P. Tribedy,[52] B. A. Trzeciak,[53] O. D. Tsai,[7] J. Turnau,[33] T. Ullrich,[4] D. G. Underwood,[2] G. Van Buren,[4] G. van Nieuwenhuizen,[26] J. A. Vanfossen, Jr.,[22] R. Varma,[17] G. M. S. Vasconcelos,[8] F. Videbæk,[4] Y. P. Viyogi,[52] S. Vokal,[21] S. A. Voloshin,[55] A. Vossen,[18] M. Wada,[47] F. Wang,[37] G. Wang,[7] H. Wang,[28] J. S. Wang,[24] Q. Wang,[37] X. L. Wang,[42] Y. Wang,[49] G. Webb,[23] J. C. Webb,[4] G. D. Westfall,[28] C. Whitten, Jr.,[7] H. Wieman,[25] S. W. Wissink,[18] R. Witt,[50] W. Witzke,[23] Y. F. Wu,[9] Z. Xiao,[49] W. Xie,[37] K. Xin,[40] H. Xu,[24] N. Xu,[25] Q. H. Xu,[43] W. Xu,[7] Y. Xu,[42] Z. Xu,[4] L. Xue,[44] Y. Yang,[24] Y. Yang,[9] P. Yepes,[40] Y. Yi,[37] K. Yip,[4] I-K. Yoo,[38] M. Zawisza,[53] H. Zbroszczyk,[53] J. B. Zhang,[9] S. Zhang,[44] W. M. Zhang,[22] X. P. Zhang,[49] Y. Zhang,[42] Z. P. Zhang,[42] F. Zhao,[7] J. Zhao,[44] C. Zhong,[44] X. Zhu,[49] Y. H. Zhu,[44] Y. Zoulkarneeva,[21] and M. Zyzak[25]

(STAR Collaboration)

[1]*AGH University of Science and Technology, Cracow, Poland*

[2]*Argonne National Laboratory, Argonne, Illinois 60439, USA*

[3]*University of Birmingham, Birmingham, United Kingdom*

[4]*Brookhaven National Laboratory, Upton, New York 11973, USA*

[5]*University of California, Berkeley, California 94720, USA*

[6]*University of California, Davis, California 95616, USA*

[7]*University of California, Los Angeles, California 90095, USA*

[8]*Universidade Estadual de Campinas, Sao Paulo, Brazil*

[9]*Central China Normal University (HZNU), Wuhan 430079, China*

[10]*University of Illinois at Chicago, Chicago, Illinois 60607, USA*

[11]*Cracow University of Technology, Cracow, Poland*
[12]*Creighton University, Omaha, Nebraska 68178, USA*
[13]*Czech Technical University in Prague, FNSPE, Prague 115 19, Czech Republic*
[14]*Nuclear Physics Institute AS CR, 250 68 Řež/Prague, Czech Republic*
[15]*University of Frankfurt, Frankfurt, Germany*
[16]*Institute of Physics, Bhubaneswar 751005, India*
[17]*Indian Institute of Technology, Mumbai, India*
[18]*Indiana University, Bloomington, Indiana 47408, USA*
[19]*Alikhanov Institute for Theoretical and Experimental Physics, Moscow, Russia*
[20]*University of Jammu, Jammu 180001, India*
[21]*Joint Institute for Nuclear Research, Dubna 141 980, Russia*
[22]*Kent State University, Kent, Ohio 44242, USA*
[23]*University of Kentucky, Lexington, Kentucky 40506-0055, USA*
[24]*Institute of Modern Physics, Lanzhou, China*
[25]*Lawrence Berkeley National Laboratory, Berkeley, California 94720, USA*
[26]*Massachusetts Institute of Technology, Cambridge, Massachusetts 02139-4307, USA*
[27]*Max-Planck-Institut für Physik, Munich, Germany*
[28]*Michigan State University, East Lansing, Michigan 48824, USA*
[29]*Moscow Engineering Physics Institute, Moscow Russia*
[30]*National Institute of Science and Education and Research, Bhubaneswar 751005, India*
[31]*Ohio State University, Columbus, Ohio 43210, USA*
[32]*Old Dominion University, Norfolk, Virginia 23529, USA*
[33]*Institute of Nuclear Physics PAN, Cracow, Poland*
[34]*Panjab University, Chandigarh 160014, India*
[35]*Pennsylvania State University, University Park, Pennsylvania 16802, USA*
[36]*Institute of High Energy Physics, Protvino, Russia*
[37]*Purdue University, West Lafayette, Indiana 47907, USA*
[38]*Pusan National University, Pusan, Republic of Korea*
[39]*University of Rajasthan, Jaipur 302004, India*
[40]*Rice University, Houston, Texas 77251, USA*
[41]*Universidade de Sao Paulo, Sao Paulo, Brazil*
[42]*University of Science & Technology of China, Hefei 230026, China*
[43]*Shandong University, Jinan, Shandong 250100, China*
[44]*Shanghai Institute of Applied Physics, Shanghai 201800, China*
[45]*SUBATECH, Nantes, France*
[46]*Texas A&M University, College Station, Texas 77843, USA*
[47]*University of Texas, Austin, Texas 78712, USA*
[48]*University of Houston, Houston, Texas 77204, USA*
[49]*Tsinghua University, Beijing 100084, China*
[50]*United States Naval Academy, Annapolis, Maryland 21402, USA*
[51]*Valparaiso University, Valparaiso, Indiana 46383, USA*
[52]*Variable Energy Cyclotron Centre, Kolkata 700064, India*
[53]*Warsaw University of Technology, Warsaw, Poland*
[54]*University of Washington, Seattle, Washington 98195, USA*
[55]*Wayne State University, Detroit, Michigan 48201, USA*
[56]*Yale University, New Haven, Connecticut 06520, USA*
[57]*University of Zagreb, Zagreb, HR-10002, Croatia*

(Received 25 June 2012; revised manuscript received 11 September 2012; published 15 November 2012)

A systematic study is presented for centrality, transverse momentum (p_T), and pseudorapidity (η) dependence of the inclusive charged hadron elliptic flow (v_2) at midrapidity ($|\eta| < 1.0$) in Au + Au collisions at $\sqrt{s_{NN}} = 7.7$, 11.5, 19.6, 27, and 39 GeV. The results obtained with different methods, including correlations with the event plane reconstructed in a region separated by a large pseudorapidity gap and four-particle cumulants ($v_2\{4\}$), are presented to investigate nonflow correlations and v_2 fluctuations. We observe that the difference between $v_2\{2\}$ and $v_2\{4\}$ is smaller at the lower collision energies. Values of v_2, scaled by the initial coordinate space eccentricity, v_2/ε, as a function of p_T are larger in more central collisions, suggesting stronger collective flow develops in more central collisions, similar to the results at higher collision energies. These results are compared to measurements at higher energies at the Relativistic Heavy Ion Collider ($\sqrt{s_{NN}} = 62.4$ and 200 GeV) and at the Large Hadron

Collider (Pb + Pb collisions at $\sqrt{s_{NN}} = 2.76$ TeV). The $v_2(p_T)$ values for fixed p_T rise with increasing collision energy within the p_T range studied (<2 GeV/c). A comparison to viscous hydrodynamic simulations is made to potentially help understand the energy dependence of $v_2(p_T)$. We also compare the v_2 results to UrQMD and AMPT transport model calculations, and physics implications on the dominance of partonic versus hadronic phases in the system created at beam energy scan energies are discussed.

DOI: 10.1103/PhysRevC.86.054908 PACS number(s): 25.75.Ld, 25.75.Dw

I. INTRODUCTION

Azimuthal anisotropies of particle distributions relative to the reaction plane (plane subtended by the impact parameter and beam direction) in high-energy heavy-ion collisions have been used to characterize the collision dynamics [1–3]. In a picture of hydrodynamic expansion of the system formed in the collisions, these anisotropies are expected to arise owing to initial pressure gradients and subsequent interactions of the constituents [4,5]. Specifically, differential measurements [6–19] of azimuthal anisotropy have been found to be sensitive to (a) the equation of state (EOS), (b) thermalization, (c) transport coefficients of the medium, and (d) initial conditions in the heavy-ion collisions. Hence, it is important to study the dependence of azimuthal anisotropy as a function of several variables, for example center-of-mass energy ($\sqrt{s_{NN}}$), collision centrality, transverse momentum (p_T), and pseudorapidity (η).

Recently, a beam-energy scan (BES) program has begun at RHIC to study the QCD phase diagram [20]. The BES program extends the baryonic chemical potential (μ_B) reach of RHIC from 20 MeV to about 400 MeV [21,22]. The baryon chemical potential decreases with the decrease in the beam energy while the chemical freeze-out temperature increases with increase in beam energy [23]. This allows one to study azimuthal anisotropy at midrapidity with varying net-baryon densities. Lattice QCD calculations suggest that the quark-hadron transition is a crossover for high-temperature (T) systems with small μ_B or high $\sqrt{s_{NN}}$ [24]. Several model calculations suggest that at larger values of μ_B or lower $\sqrt{s_{NN}}$ the transition is expected to be first order [25–27]. Theoretical calculations suggest a nonmonotonic behavior of v_2 could be observed around this "softest point of the EOS" [28]. The softest point of the EOS is usually referred to as the temperature/time during which the velocity of sound has a minimum value (or reduction in the pressure of the system) during the evolution. Nonmonotonic variation of azimuthal anisotropy as a function of collision centrality and $\sqrt{s_{NN}}$ could indicate the softest point of the EOS in heavy-ion reactions [29]. Further, it has been argued that the observation of saturation of differential azimuthal anisotropies $v_2(p_T)$ of charged hadrons in Au + Au collisions in the $\sqrt{s_{NN}}$ range of 62.4–200 GeV is a signature of a mixed phase [15]. The new data presented in this paper shows to what extent such a saturation effect is observed.

Several analysis methods for v_2 have been proposed [30–34]. These are found to be sensitive in varying degrees to nonflow contributions (e.g., correlations owing to jets, resonances, etc.) and flow fluctuations. v_2 measurements from various methods have been judiciously used to constrain these contributions, in addition to providing estimates of systematic errors associated with the measurements [35]. This is particularly useful for interpreting results of identified hadron v_2 values where, owing to limitations of event statistics, it is not possible to use all methods for v_2 analysis. The measurements over a range of energies may provide insights to the evolution of nonflow and flow fluctuations as a function of collision energy.

Inclusive charged hadron elliptic flow measurements at top RHIC energies have been one of the most widely studied observables from the theoretical perspective. It has been shown that transport models, which provide a microscopic description of the early and late nonequilibrium stages of the system, significantly underpredict v_2 at top RHIC energies, while the inclusion of partonic effects provides a more satisfactory explanation [36]. The new data discussed here will provide an opportunity to study the contribution of partonic matter and hadronic matter to the v_2 measurements as a function of $\sqrt{s_{NN}}$ or (T, μ_B) by comparisons with models.

In this paper we present measurements of the second harmonic azimuthal anisotropy using data taken in the BES program from $\sqrt{s_{NN}} = 7.7$ to 39 GeV. We discuss the detectors used in the analysis, data selections, and methods used to determine inclusive charged hadron v_2 in Secs. II and III. Section IV gives v_2 results for inclusive charged hadrons from different analysis methods. We discuss the centrality, η, p_T, and $\sqrt{s_{NN}}$ dependence of v_2 in Sec. V and compare to calculations from transport models. Finally, a summary of the analysis is presented in Sec. VI.

II. EXPERIMENTS AND DATA SETS

A. STAR detector

The results presented here are based on data collected during the 10th and 11th RHIC runs (2010 and 2011) with the STAR detector using minimum-bias triggers (requiring a combination of signals from the beam-beam counters (BBCs) [37], zero-degree calorimeters (ZDCs) [38], and vertex position detectors (VPDs) [39]). For the 7.7- and 11.5-GeV data, at least one hit in the full barrel time-of-flight detector [40] was required to further reduce the background. The main time projection chamber (TPC) [41] and two forward time projection chambers (FTPCs) [42] were used for particle tracking in the central region ($|\eta| < 1.0$) and forward regions ($2.5 < |\eta| < 4.0$), respectively. Both the TPC and the FTPCs provided azimuthal acceptance over 2π. The BBC detector subsystem consists of two detectors mounted around the beam pipe, each located outside the STAR magnet pole tip at opposite ends of the TPC approximately 375 cm from the center of the nominal interaction point. Each BBC detector consists of hexagonal scintillator tiles arranged in four concentric rings

that provided full azimuthal coverage. The inner tiles of the BBCs, with a pseudorapidity range of $3.8 < |\eta| < 5.2$ were used to reconstruct the event plane in one elliptic flow analysis.

B. Event and track selection

Events for analysis are selected based on collision vertex positions within 2 cm of the beam axis to reduce contributions from beam-gas and beam-pipe (at a radius of 4 cm) interactions, and within a limited distance from the center of the detector along the beam direction (± 70 cm for the 7.7-GeV data set, ± 50 cm for the 11.5-GeV data set, and ± 40 cm for the 19.6-, 27-, and 39-GeV data sets). These values are chosen to reduce systematics owing to variance in detector performance over $|\eta| < 1.0$ while retaining sufficient statistics. After quality cuts, about 4×10^6 0%–80% central events remain for 7.7 GeV, 11×10^6 for 11.5 GeV, 20×10^6 for 19.6 GeV, 40×10^6 for 27 GeV, and 120×10^6 for 39 GeV data sets. The results from more peripheral collisions are not presented owing to trigger inefficiencies at low multiplicity. The centrality was defined using the number of charged tracks with quality cuts similar to those in Ref. [12]. The details of the centrality determination is discussed in Part C of this section. The 0%–80% central events for v_2 analysis of charged hadrons are divided into nine centrality bins: 0%–5%, 5%–10%, 10%–20%, 20%–30%, 30%–40%, 40%–50%, 50%–60%, 60%–70%, and 70%–80%.

A variety of track quality cuts are used to select good charged particle tracks reconstructed using information from the TPC or FTPCs. The distance of closest approach (DCA) of the track to the primary vertex is taken to be less than 2 cm. We require that the TPC and FTPCs have a number of fit points used for reconstruction of the tracks to be >15 and >5, respectively. For the TPC and FTPCs the ratio of the number of fit points to maximum possible hits is >0.52. An additional transverse momentum cut ($0.2 < p_T < 2$ GeV/c) is applied to the charged tracks for the TPC and FTPC event-plane determination.

C. Centrality determination

The centrality classes are defined based on the uncorrected charged-particle multiplicity ($N_{\rm ch}^{\rm raw}$) distribution in the TPC for pseudorapidity $|\eta| < 0.5$ and full azimuth.

Figure 1 shows the $N_{\rm ch}^{\rm raw}$ distribution for charged particles from the data at $\sqrt{s_{NN}} = 7.7$, 11.5, 19.6, 27, and 39 GeV compared to those from Monte Carlo (MC) Glauber simulations. The detailed procedures to obtain the simulated multiplicity are similar to that described in Ref. [43]. A two-component model [44] is used to calculate the simulated multiplicity distribution given by

$$\left.\frac{dN_{\rm ch}}{d\eta}\right|_{\eta=0} = n_{pp}\left[(1-x)\frac{N_{\rm part}}{2} + xN_{\rm coll}\right], \qquad (1)$$

where $N_{\rm part}$ is the number of participant nucleons and $N_{\rm coll}$ is the number of binary nucleon-nucleon collisions in the simulations. The fitting parameter n_{pp} is the average multiplicity per unit of pseudorapidity in minimum-bias $p + p$ collisions and x is the fraction of production from the hard component.

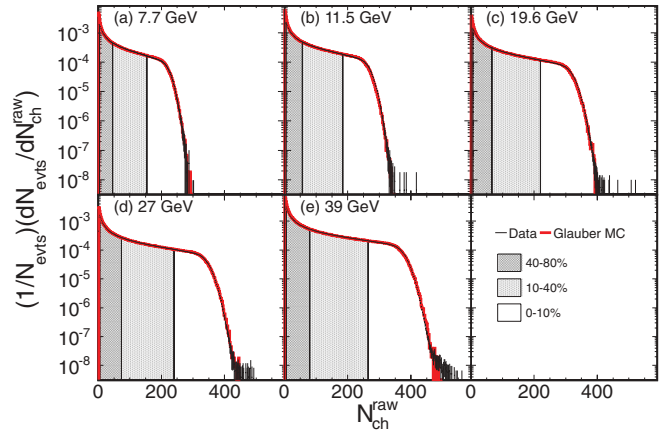

FIG. 1. (Color online) Distribution of uncorrected multiplicity $N_{\rm ch}^{\rm raw}$ measured within $|\eta| < 0.5$ in the TPC from $\sqrt{s_{NN}} = 7.7$ to 39 GeV in Au + Au collisions shown as black points. The red curves show the multiplicity distributions at $\sqrt{s_{NN}} = 7.7$ to 39 GeV from MC Glauber simulations. See text for more details about simulations.

The inelastic nucleon-nucleon cross section $\sigma_{NN}^{\rm inel}$ is extracted from fitting the results of available data for total and elastic $p + p$ cross sections from the Particle Data Group [45]. The x value is fixed at 0.12 ± 0.02 based on the linear interpolation of the PHOBOS results at $\sqrt{s_{NN}} = 19.6$ and 200 GeV [46]. Systematic errors on n_{pp} are evaluated by varying both n_{pp} and x within the quoted x uncertainty to determine the minimum χ^2 to describe the data. Because the n_{pp} and x are anticorrelated, lower (higher) n_{pp} is used for higher (lower) x for systematic error evaluations on $N_{\rm part}$. Table I summarizes the parameters in the two-component model and $\sigma_{NN}^{\rm inel}$ in the MC Glauber simulations. The event-by-event multiplicity fluctuations are included using negative binomial distributions [43]. The centrality classes are defined by the fractions of geometrical cross section from the simulated multiplicity distributions. For each centrality bin, average quantities are calculated in the MC Glauber simulations for $\langle N_{\rm part}\rangle$, $\langle N_{\rm coll}\rangle$, reaction plane eccentricity $\langle \varepsilon_{\rm RP}\rangle$, participant eccentricity $\langle \varepsilon_{\rm part}\rangle$, root-mean-square participant eccentricity $\varepsilon_{\rm part}\{2\}$, and transverse area $\langle S_{\rm part}\rangle$. Eccentricity and transverse area are defined by

$$\varepsilon_{\rm RP} = \frac{\sigma_y^2 - \sigma_x^2}{\sigma_x^2 + \sigma_y^2}, \qquad (2)$$

TABLE I. Summary of n_{pp} and $\sigma_{NN}^{\rm inel}$ with systematic uncertainties at $\sqrt{s_{NN}} = 7.7$, 11.5, 19.6, 27, and 39 GeV. x is set to 0.12 ± 0.02 for all collision energies.

$\sqrt{s_{NN}}$ (GeV)	n_{pp}	$\sigma_{NN}^{\rm inel}$ (mb)
7.7	0.89 ± 0.04	30.8 ± 1.0
11.5	1.07 ± 0.05	31.2 ± 1.0
19.6	1.29 ± 0.05	32.0 ± 1.0
27	1.39 ± 0.06	33.0 ± 1.0
39	1.52 ± 0.08	34.0 ± 1.0

$$\varepsilon_{\rm part} = \frac{\sqrt{\left(\sigma_y^2 - \sigma_x^2\right)^2 + 4\sigma_{xy}^2}}{\sigma_x^2 + \sigma_y^2}, \quad \varepsilon_{\rm part}\{2\} = \sqrt{\langle \varepsilon_{\rm part}^2 \rangle}, \tag{3}$$

$$S_{\rm part} = \pi \sqrt{\sigma_x^2 \sigma_y^2 - \sigma_{xy}^2}, \tag{4}$$

$$\sigma_x^2 = \{x^2\} - \{x\}^2, \quad \sigma_y^2 = \{y^2\} - \{y\}^2, \tag{5}$$

$$\sigma_{xy} = \{xy\} - \{x\}\{y\}, \tag{6}$$

where the curly brackets denote the average over all participants per event and x and y are the positions of participant nucleons. Systematic uncertainties on those quantities are evaluated by varying parameters for the two-component model and by varying the input parameters in the MC Glauber model. The quoted errors are the quadratic sum of the individual systematic uncertainties. Table II summarizes the centrality classes as well as the results obtained by MC Glauber simulations at the five energies.

III. ELLIPTIC FLOW METHODS

A. The event-plane method

The event-plane method [30] correlates each particle with the event plane determined from the full event minus the particle of interest, which can be done for each harmonic. For any Fourier harmonic, n, the event flow vector (Q_n) and the event-plane angle (Ψ_n) are defined by [30]

$$Q_n \cos n\Psi_n = Q_{nx} = \sum_i w_i \cos n\phi_i, \tag{7}$$

$$Q_n \sin n\Psi_n = Q_{ny} = \sum_i w_i \sin n\phi_i, \tag{8}$$

$$\Psi_n = \left(\tan^{-1}\frac{Q_{ny}}{Q_{nx}}\right) \Big/ n, \tag{9}$$

where sums extend over all particles i used in the event-plane calculation, and ϕ_i and w_i are the laboratory azimuthal angle and the weight for the ith particle, respectively. The reaction plane azimuthal distribution should be isotropic or flat in the laboratory frame if the detectors have ideal acceptance. Because the detectors usually have nonuniform acceptance, a procedure for flattening the laboratory event-plane distribution is necessary [47,48].

As shown in Eq. (10), the observed v_2 is calculated with respect to the reconstructed event-plane angle Ψ_n, where n equals 2 when we use the second harmonic event plane and n equals 1 when we use the first harmonic event plane:

$$v_2^{\rm obs} = \langle \cos[2(\phi - \Psi_n)] \rangle. \tag{10}$$

The angular brackets indicate an average over all particles in all events. However, tracks used for the v_2 calculation are excluded from the calculation of the flow vector to remove self-correlation effects. Because the estimated reaction plane fluctuates owing to finite number of particles, one has to correct for this smearing by dividing the observed correlation by the event-plane resolution [the denominator in Eq. (11)], which is the correlation of the event plane with the reaction plane:

$$v_2 = \frac{v_2^{\rm obs}}{\langle \cos[2(\Psi_n - \Psi_r)] \rangle}. \tag{11}$$

Because the reaction plane is unknown, the denominator in Eq. (11) could not be calculated directly. As shown in Eq. (12), we estimate the event-plane resolution by the correlation between the azimuthal angles of two subset groups of tracks, called subevents A and B. In Eq. (12) C is a factor calculated from the known multiplicity dependence of the resolution [30]:

$$\langle \cos[2(\Psi_n - \Psi_r)] \rangle = C \sqrt{\left\langle \cos\left[2\left(\Psi_n^A - \Psi_n^B\right)\right]\right\rangle}. \tag{12}$$

Random subevents are used for TPC event plane, while pseudorapidity subevents are used for FTPC/BBC event plane.

1. TPC event plane

The TPC event plane means the event plane reconstructed from tracks recorded by the TPC. For this event plane the ϕ weight method is an effective way to flatten the azimuthal distribution for removing detector acceptance bias. These weights are generated by inverting the ϕ distributions of detected tracks for a large event sample. The ϕ weights are folded into the weight w_i in Eqs. (7) and (8).

The recentering correction [47,48] is another method to calibrate the event plane. In this method, one subtracts from the Q vector of each event the Q vector averaged over many events. For both the ϕ weight and recentering methods, the corrections are applied in each centrality bin, in two bins of the primary vertex position along the longitudinal beam direction (V_z), and in two bins for positive/negative pseudorapidity. These corrections are determined as a function of data collection time. The difference in the effects on v_2 from the different flattening techniques is negligible.

2. FTPC event plane

Forward-going tracks reconstructed in the two FTPCs can also be used to determine the event plane. However, large acceptance losses from hardware faults caused significant gaps in the azimuthal angle distribution of these tracks, preventing use of the ϕ weight method because of the inability to define ϕ weights in regions of zero acceptance. Thus, only the recentering method is used for the FTPC.

3. BBC event plane

In this method the first-order event plane is reconstructed using particle trajectories determined from hits in the BBC detectors. In this case, ϕ_i denotes the fixed azimuthal angle of the center of the ith BBC tile in Eqs. (7) and (8), and w_i is the fraction of BBC-observed energy deposition recorded in tile i:

$$w_i = \frac{A_i}{\sum A_i}. \tag{13}$$

TABLE II. Summary of centrality bins, average number of participants $\langle N_{\rm part}\rangle$, number of binary collisions $\langle N_{\rm coll}\rangle$, reaction plane eccentricity $\langle\varepsilon_{\rm RP}\rangle$, participant eccentricity $\langle\varepsilon_{\rm part}\rangle$, root-mean-square the participant eccentricity $\varepsilon_{\rm part}\{2\}$, and transverse area $\langle S_{\rm part}\rangle$ from MC Glauber simulations at $\sqrt{s_{NN}}$ = 7.7, 11.5, 19.6, 27, and 39 GeV. The errors are systematic uncertainties.

Centrality (%)	$\langle N_{\rm part}\rangle$	$\langle N_{\rm coll}\rangle$	$\langle\varepsilon_{\rm RP}\rangle$	$\langle\varepsilon_{\rm part}\rangle$	$\varepsilon_{\rm part}\{2\}$	$\langle S_{\rm part}\rangle$ (fm^2)
			Au + Au at $\sqrt{s_{NN}} = 7.7$ GeV			
0–5	337 ± 2	774 ± 28	0.043 ± 0.007	0.102 ± 0.003	0.117 ± 0.003	25.5 ± 0.4
5–10	290 ± 6	629 ± 20	0.10 ± 0.01	0.14 ± 0.01	0.16 ± 0.01	23.0 ± 0.3
10–20	226 ± 8	450 ± 22	0.18 ± 0.02	0.21 ± 0.02	0.24 ± 0.02	19.5 ± 0.4
20–30	160 ± 10	283 ± 24	0.26 ± 0.03	0.30 ± 0.02	0.32 ± 0.02	15.7 ± 0.7
30–40	110 ± 11	171 ± 23	0.32 ± 0.04	0.37 ± 0.03	0.39 ± 0.03	12.6 ± 0.8
40–50	72 ± 10	96 ± 19	0.36 ± 0.04	0.43 ± 0.03	0.46 ± 0.03	10.0 ± 0.9
50–60	45 ± 9	52 ± 13	0.39 ± 0.04	0.50 ± 0.03	0.53 ± 0.03	7.8 ± 1.0
60–70	26 ± 7	25 ± 9	0.40 ± 0.05	0.58 ± 0.04	0.62 ± 0.04	5.8 ± 1.1
70–80	14 ± 4	12 ± 5	0.36 ± 0.05	0.68 ± 0.04	0.72 ± 0.04	3.6 ± 1.0
			Au + Au at $\sqrt{s_{NN}} = 11.5$ GeV			
0–5	338 ± 2	784 ± 27	0.043 ± 0.006	0.102 ± 0.003	0.116 ± 0.003	25.6 ± 0.4
5–10	290 ± 6	635 ± 20	0.10 ± 0.01	0.14 ± 0.01	0.16 ± 0.01	23.0 ± 0.3
10–20	226 ± 8	453 ± 23	0.18 ± 0.02	0.22 ± 0.02	0.24 ± 0.02	19.5 ± 0.5
20–30	160 ± 9	284 ± 23	0.26 ± 0.03	0.30 ± 0.02	0.32 ± 0.02	15.7 ± 0.7
30–40	110 ± 10	172 ± 22	0.32 ± 0.04	0.37 ± 0.03	0.39 ± 0.03	12.6 ± 0.8
40–50	73 ± 10	98 ± 18	0.36 ± 0.04	0.43 ± 0.03	0.46 ± 0.03	10.1 ± 0.9
50–60	44 ± 9	52 ± 14	0.39 ± 0.04	0.50 ± 0.03	0.53 ± 0.03	7.8 ± 1.0
60–70	26 ± 7	25 ± 9	0.40 ± 0.05	0.58 ± 0.04	0.62 ± 0.04	5.8 ± 1.1
70–80	14 ± 6	12 ± 6	0.37 ± 0.06	0.68 ± 0.05	0.71 ± 0.05	3.7 ± 1.2
			Au + Au at $\sqrt{s_{NN}} = 19.6$ GeV			
0–5	338 ± 2	800 ± 27	0.044 ± 0.006	0.102 ± 0.003	0.117 ± 0.003	25.6 ± 0.4
5–10	289 ± 6	643 ± 20	0.11 ± 0.01	0.15 ± 0.01	0.16 ± 0.01	23.0 ± 0.3
10–20	225 ± 9	458 ± 24	0.18 ± 0.02	0.22 ± 0.02	0.24 ± 0.02	19.5 ± 0.5
20–30	158 ± 10	284 ± 26	0.26 ± 0.03	0.30 ± 0.02	0.32 ± 0.02	15.6 ± 0.7
30–40	108 ± 10	170 ± 23	0.32 ± 0.04	0.37 ± 0.03	0.40 ± 0.03	12.5 ± 0.8
40–50	71 ± 10	96 ± 18	0.36 ± 0.04	0.43 ± 0.03	0.46 ± 0.03	10.0 ± 0.9
50–60	44 ± 9	51 ± 13	0.39 ± 0.04	0.50 ± 0.03	0.53 ± 0.03	7.8 ± 1.0
60–70	25 ± 7	25 ± 8	0.40 ± 0.05	0.58 ± 0.04	0.62 ± 0.04	5.8 ± 1.1
70–80	14 ± 5	12 ± 5	0.37 ± 0.06	0.68 ± 0.05	0.71 ± 0.05	3.7 ± 1.2
			Au + Au at $\sqrt{s_{NN}} = 27$ GeV			
0–5	343 ± 2	841 ± 28	0.040 ± 0.005	0.100 ± 0.002	0.114 ± 0.003	25.8 ± 0.4
5–10	299 ± 6	694 ± 22	0.10 ± 0.01	0.14 ± 0.01	0.16 ± 0.01	23.4 ± 0.3
10–20	233 ± 9	497 ± 26	0.18 ± 0.02	0.21 ± 0.02	0.23 ± 0.02	19.8 ± 0.5
20–30	166 ± 11	312 ± 28	0.26 ± 0.03	0.29 ± 0.02	0.32 ± 0.02	15.9 ± 0.7
30–40	114 ± 11	188 ± 25	0.32 ± 0.04	0.37 ± 0.03	0.39 ± 0.03	12.8 ± 0.9
40–50	75 ± 10	106 ± 20	0.37 ± 0.04	0.43 ± 0.03	0.46 ± 0.03	10.2 ± 0.9
50–60	47 ± 9	56 ± 15	0.39 ± 0.05	0.50 ± 0.03	0.53 ± 0.03	7.9 ± 1.0
60–70	27 ± 8	27 ± 10	0.40 ± 0.05	0.58 ± 0.05	0.61 ± 0.05	5.8 ± 1.2
70–80	14 ± 6	12 ± 6	0.37 ± 0.06	0.68 ± 0.05	0.71 ± 0.05	3.6 ± 1.3
			Au + Au at $\sqrt{s_{NN}} = 39$ GeV			
0–5	342 ± 2	853 ± 27	0.042 ± 0.006	0.101 ± 0.003	0.115 ± 0.003	25.9 ± 0.4
5–10	294 ± 6	687 ± 21	0.10 ± 0.01	0.14 ± 0.01	0.16 ± 0.01	23.3 ± 0.3
10–20	230 ± 9	492 ± 26	0.18 ± 0.02	0.21 ± 0.02	0.23 ± 0.02	19.8 ± 0.5
20–30	162 ± 10	306 ± 27	0.26 ± 0.03	0.30 ± 0.02	0.32 ± 0.02	16.0 ± 0.7
30-40	111 ± 11	183 ± 24	0.32 ± 0.04	0.37 ± 0.03	0.39 ± 0.03	12.8 ± 0.8
40–50	74 ± 10	104 ± 20	0.36 ± 0.04	0.43 ± 0.03	0.46 ± 0.03	10.3 ± 1.0
50–60	46 ± 9	55 ± 14	0.39 ± 0.04	0.50 ± 0.03	0.53 ± 0.03	8.0 ± 1.0
60–70	26 ± 7	27 ± 9	0.40 ± 0.04	0.58 ± 0.04	0.61 ± 0.04	5.9 ± 1.1
70–80	14 ± 5	12 ± 6	0.37 ± 0.05	0.67 ± 0.05	0.71 ± 0.05	3.8 ± 1.2

The BBC event plane obtained from one BBC detector is called a subevent. A combination of the subevent-plane vectors for both BBC detectors provides the full event plane,

$$v_2\{\mathrm{BBC}\} = \frac{\langle \cos[2(\phi - \Psi_1)]\rangle}{C\sqrt{\langle \cos\left[2\left(\Psi_1^A - \Psi_1^B\right)\right]\rangle}}, \tag{14}$$

where C is the constant in Eq. (12). Ψ_1^A, Ψ_1^B are subevent-plane angles from each BBC detector and Ψ_1 is the full event-plane angle from both subevents combined.

The detector acceptance bias is removed by applying the shift method [48]. Equation (15) shows the formula for the shift correction. The averages in Eq. (15) are taken from a large sample of events. In this analysis, the correction is done up to the 20th harmonic. The distributions of Ψ_1^{A} and Ψ_1^{B} are separately flattened and then the full-event event-plane distribution is flattened. Accordingly, the observed v_2 and resolution are calculated using the shifted (sub)event-plane azimuthal angles:

$$\Psi' = \Psi + \sum_n \frac{1}{n}[-\langle \sin(2n\Psi)\rangle \cos(2n\Psi) + \langle \cos(2n\Psi)\rangle \sin(2n\Psi)]. \tag{15}$$

More details for the BBC event plane have been described in Ref. [49].

B. The η subevent method

The η subevent method is similar to the event-plane method, except one defines the flow vector for each particle based on particles measured in the opposite hemisphere in pseudorapidity:

$$v_2\{\mathrm{EtaSubs}\} = \frac{\langle \cos[2(\phi_\pm - \Psi_{2,\eta_\mp})]\rangle}{\sqrt{\langle \cos[2(\Psi_{2,\eta_+} - \Psi_{2,\eta_-})]\rangle}}. \tag{16}$$

Here $v_2\{\mathrm{EtaSubs}\}$ denotes the results of the η subevent method and $\Psi_{2,\eta_+}(\Psi_{2,\eta_-})$ is the second harmonic event-plane angle determined by particles with positive (negative) pseudorapidity. An η gap of $|\eta| < 0.075$ is used between negative (positive) η subevents to reduce nonflow correlations between the two ensembles.

C. The cumulant method

The advantage of the cumulant method is that the multiparticle cumulant is a higher-order multiparticle correlation formalism which removes the contribution of nonflow correlations from lower-order correlations [32,33]. The measured two-particle correlations can be expressed with flow and nonflow components:

$$\langle e^{in(\phi_1-\phi_2)}\rangle = \langle e^{in(\phi_1-\Psi_r)}\rangle\langle e^{in(\Psi_r-\phi_2)}\rangle + \delta_n = v_n^2 + \delta_n. \tag{17}$$

Here n is the harmonic number and δ_n denotes the nonflow contribution. The average should be taken for all pairs of particles in a certain rapidity and transverse momentum region and for all events of a data sample. The measured four-particle correlations can be expressed as

$$\langle e^{in(\phi_1+\phi_2-\phi_3-\phi_4)}\rangle = v_n^4 + 2\times 2\times v_n^2\delta_n + 2\delta_n^2. \tag{18}$$

Thus, the flow contribution can be obtained by subtracting the two-particle correlation from the four-particle correlation,

$$\langle\langle e^{in(\phi_1+\phi_2-\phi_3-\phi_4)}\rangle\rangle = \langle e^{in(\phi_1+\phi_2-\phi_3-\phi_4)}\rangle - 2\langle e^{in(\phi_1-\phi_3)}\rangle^2 = -v_n^4, \tag{19}$$

where $\langle\langle\cdots\rangle\rangle$ is used for the cumulant. The cumulant of order two is just $\langle\langle e^{in(\phi_1-\phi_2)}\rangle\rangle = \langle e^{in(\phi_1-\phi_2)}\rangle$.

1. The cumulant method with generating function

The GF-cumulant method is computed from a generating function [33]:

$$G_n(z) = \prod_{j=1}^{M}\left[1 + \frac{w_j}{M}(z^* e^{in\phi_j} + z e^{-in\phi_j})\right]. \tag{20}$$

Here z is an arbitrary complex number, z^* denotes its complex conjugate, M denotes the multiplicity in each event, and w_j is the weight (transverse momentum, rapidity, etc.) used in the analysis. The eventwise averaged generating function then can be expanded in powers of z and z^* where the coefficients of expansion yield the correlations of interest:

$$\langle G_n(z)\rangle = 1 + z\langle e^{-in\phi_1}\rangle + z^*\langle e^{in\phi_1}\rangle + \frac{M-1}{M}\left(\frac{z^2}{2}\langle e^{-in(\phi_1+\phi_2)}\rangle + \frac{z^{*2}}{2}\langle e^{in(\phi_1+\phi_2)}\rangle + zz^*\langle e^{in(\phi_1-\phi_2)}\rangle\right) + \cdots. \tag{21}$$

These correlations can be used to construct the cumulants. More details for the analysis of STAR data have been described in Ref. [10].

2. The Q-cumulants method

The Q-cumulants method [50] is a recent method to calculate cumulants without using nested loops over tracks and without generating functions [33]. The advantage is that it provides fast (one loop over data) and exact nonbiased (no approximations and no interference between different harmonics) estimates of the correlators compared to the generating function cumulants. The cumulants are expressed in terms of the moments of the magnitude of the corresponding flow vector Q_n

$$Q_n \equiv \sum_{i=1}^{M} e^{in\phi_i}. \tag{22}$$

The single-event average two- and four-particle azimuthal correlations can be then formulated as

$$\langle 2\rangle = \frac{|Q_n|^2 - M}{M(M-1)} \tag{23}$$

$$\langle 4\rangle = \frac{|Q_n|^4 + |Q_{2n}|^2 - 2\mathrm{Re}[Q_{2n}Q_n^*Q_n^*]}{M(M-1)(M-2)(M-3)} - 2\frac{2(M-2)|Q_n|^2 - M(M-3)}{M(M-1)(M-2)(M-3)} \tag{24}$$

The average over all events can be performed as

$$\langle\langle 2\rangle\rangle \equiv \langle\langle e^{in(\phi_1-\phi_2)}\rangle\rangle \equiv \frac{\sum_{\text{event}}(W_{\langle 2\rangle})_i\langle 2\rangle_i}{\sum_{\text{event}}(W_{\langle 2\rangle})_i}, \tag{25}$$

$$\langle\langle 4\rangle\rangle \equiv \langle\langle e^{in(\phi_1+\phi_2-\phi_3-\phi_4)}\rangle\rangle \equiv \frac{\sum_{\text{events}}(W_{\langle 4\rangle})_i\langle 4\rangle_i}{\sum_{\text{events}}(W_{\langle 4\rangle})_i}, \tag{26}$$

while the weights are the number of two- and four-particle combinations:

$$W_{\langle 2\rangle} \equiv M(M-1), \tag{27}$$

$$W_{\langle 4\rangle} \equiv M(M-1)(M-2)(M-3). \tag{28}$$

Choosing the multiplicity weights above can make the final multiparticle azimuthal correlations free of multiplicity fluctuations [51]. However, one can also use unit weights treating events with different multiplicity equally. The two- and four-particle cumulants without detector bias then can be formulated as

$$c_n\{2\} = \langle\langle 2\rangle\rangle, \tag{29}$$

$$c_n\{4\} = \langle\langle 4\rangle\rangle - 2\times\langle\langle 2\rangle\rangle^2. \tag{30}$$

The reference flow (e.g., integrated over p_T) can be estimated both from two- and four-particle cumulants:

$$v_n\{2\} = \sqrt{c_n\{2\}}, \tag{31}$$

$$v_n\{4\} = \sqrt[4]{-c_n\{4\}}. \tag{32}$$

Once the reference flow is estimated, we proceed to the calculation of differential flow (e.g., as a function of p_T) of the particle of interest (POI), which needs another two vectors p and q. Particles used to estimate reference flow are called reference particles (REPs). For particles labeled as POI,

$$p_n \equiv \sum_{i=1}^{m_p} e^{in\psi_i}. \tag{33}$$

For particles labeled as both POI and REP,

$$q_n \equiv \sum_{i=1}^{m_p} e^{in\psi_i}. \tag{34}$$

Then the reduced single-event average two- and four-particle correlations are

$$\langle 2'\rangle = \frac{p_nQ_n^* - m_q}{m_pM - m_q}, \tag{35}$$

$$\begin{aligned}\langle 4'\rangle = [&p_nQ_nQ_n^*Q_n^* - q_{2n}Q_n^*Q_n^* - p_nQ_nQ_{2n}^* - 2Mp_nQ_n^*\\ &-2m_q|Q_n|^2 + 7q_nQ_n^* - Q_nq_n^* + q_{2n}Q_{2n}^* + 2p_nQ_n^*\\ &+2m_qM - 6m_q]/[(m_pM - 3m_q)(M-1)(M-2)].\end{aligned} \tag{36}$$

The event average can be obtained as follows:

$$\langle\langle 2'\rangle\rangle = \frac{\sum_{\text{events}}(w_{\langle 2'\rangle})_i\langle 2'\rangle_i}{\sum_{i=1}^{N}(w_{\langle 2'\rangle})_i}, \tag{37}$$

$$\langle\langle 4'\rangle\rangle = \frac{\sum_{\text{events}}(w_{\langle 4'\rangle})_i\langle 4'\rangle_i}{\sum_{i=1}^{N}(w_{\langle 4'\rangle})_i}. \tag{38}$$

Multiplicity weights are

$$w_{\langle 2'\rangle} \equiv m_pM - m_q, \tag{39}$$

$$w_{\langle 4'\rangle} \equiv (m_pM - m_q)(M-1)(M-2). \tag{40}$$

The two- and four-particle differential cumulants without detector bias are given by

$$d_n\{2\} = \langle\langle 2'\rangle\rangle, \tag{41}$$

$$d_n\{4\} = \langle\langle 4'\rangle\rangle - 2\times\langle\langle 2'\rangle\rangle\langle\langle 2\rangle\rangle. \tag{42}$$

Equations for the case of detectors without uniform acceptance can be found in Ref. [50]. Estimations of differential flow are expressed as

$$v_n'\{2\} = \frac{d_n\{2\}}{\sqrt{c_n\{2\}}}, \tag{43}$$

$$v_n'\{4\} = \frac{d_n\{4\}}{-c_n\{2\}^{3/4}}. \tag{44}$$

IV. RESULTS

A. The event-plane resolution

To investigate the nonflow correlations and v_2 fluctuations of the v_2 measurements, the event planes from different detectors and the cumulant method are used in the analysis. The event planes are determined from the TPC in the midrapidity region, and the FTPC/BBC at forward rapidity. The η gap between FTPC/BBC to TPC could reduce the nonflow contribution in the v_2 measurement [13]. Figure 2 shows the

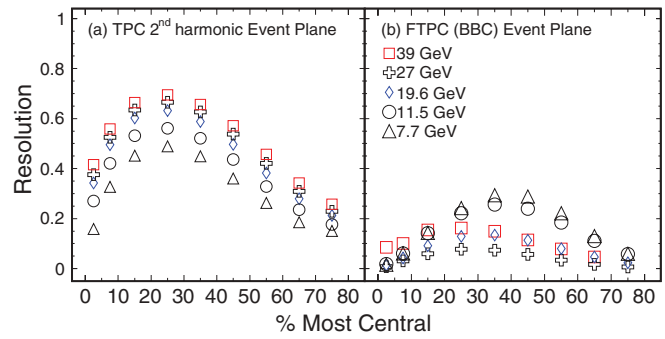

FIG. 2. (Color online) The event-plane resolutions for Au + Au collisions at $\sqrt{s_{NN}} = 7.7$, 11.5, 19.6, 27, and 39 GeV as a function of collision centrality. Panel (a) shows the resolution of the second harmonic event plane from the TPC ($|\eta| < 1$). Panel (b) shows the resolution for second harmonic event plane from the FTPCs ($2.5 < |\eta| < 4.0$) for 39 GeV and second harmonic event-plane resolution correction using the first-order event plane from the BBCs ($3.8 < |\eta| < 5.2$) for 7.7, 11.5, 19.6, and 27 GeV.

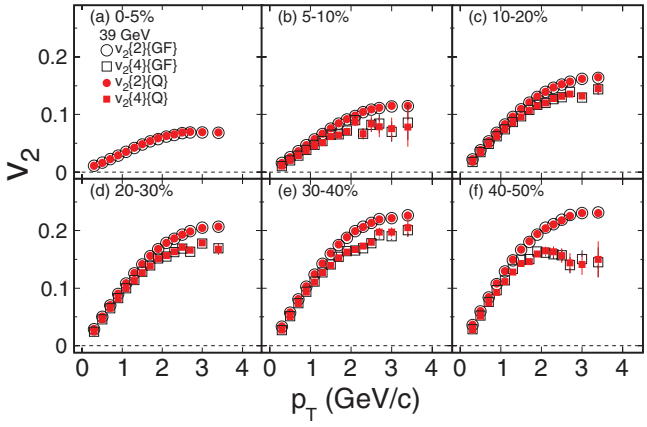

FIG. 3. (Color online) The comparison of v_2 as a function of p_T between GF-cumulant (open symbols) and Q-cumulant (solid symbols) methods in Au + Au collisions at $\sqrt{s_{NN}} = 39$ GeV. $v_2\{4\}$ fails in most central (0%–5%) collisions owing to the small values of v_2 and large v_2 fluctuations.

event-plane resolution from TPC [panel (a)] and BBC (FTPC) [panel (b)]. The resolution of the TPC second harmonic event plane increases as the collision energy increases, as the resolution depends on the multiplicity and the v_2 signal [30]. Owing to limited statistics, the FTPC event plane is used only for the 39-GeV data set where the BBC event plane cannot be used because of the poor resolution. The resolution of the FTPC event plane is about four times lower than the TPC event plane. The BBC is used to determine the event plane for the 7.7-, 11.5-, 19.6-, and 27-GeV data sets. Note the BBC event plane is based on the first harmonic, as the v_1 signal is significant in the rapidity region covered by the BBC. The qualitively different centrality dependence of the FTPC and BBC event-plane resolutions is because of the different centrality dependence of v_1 and v_2.

B. Method comparison

The comparison of v_2 as a function of p_T between the GF-cumulant and Q-cumulant methods is shown in Fig. 3 for six collision centralities in Au + Au collisions at $\sqrt{s_{NN}} = 39$ GeV. The GF-cumulant and Q-cumulant methods agree within 5% at all five collision energies. Compared to the GF-cumulant method, the recently developed Q cumulant is the exact cumulant method [50]. The observation of consistency between the two methods at BES energies implies that the GF cumulant is a good approximation. The cumulant method (GF cumulant or Q cumulant) used in the analysis does not cause difference in the comparison with other experimental results and theoretical calculations. To be consistent with the previous STAR results, we hereafter show only results from the GF-cumulant method.

Other method comparisons are shown in Figs. 4 and 5 for inclusive charged hadrons in Au + Au collisions at $\sqrt{s_{NN}} = 7.7$ GeV (a1), 11.5 GeV (b1), 19.6 GeV (c1), 27 GeV (d1), and 39 GeV (e1). As the v_2 measurements from various methods are obtained using charged tracks recorded at midrapidity ($|\eta| < 1$), the statistical errors on the results from the different v_2 methods are thus correlated. The conclusions on the differences in v_2 values from different methods are based on the systematic trends observed for the corresponding ratios with respect to $v_2\{2\}$. Figure 4 shows v_2 integrated over $0.2 < p_T < 2.0\,\mathrm{GeV}/c$ and $|\eta| < 1$ versus centrality. For comparison purposes, the integrated v_2 values for all methods are divided by the values of the two-particle cumulant method ($v_2\{2\}$) and plotted in panels (a2) through (e2). The results of the four-particle cumulants are systematically lower than the other methods, except for $v_2\{\mathrm{FTPC/BBC}\}$. The difference is about 10%–20% in 39, 27, and 19.6 GeV, 10%–15% in 11.5 GeV and 5%–10% in 7.7 GeV. The η subevent values for peripheral collisions (50%–60% to 70%–80%) drop below the two-particle and TPC event-plane results, indicating the η subevent method could reduce some nonflow

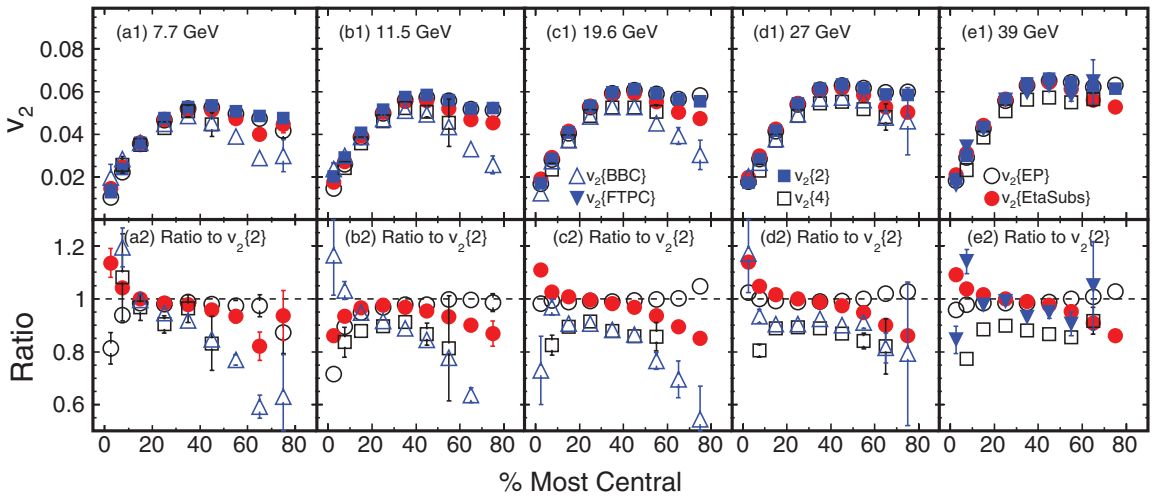

FIG. 4. (Color online) The p_T (>0.2 GeV/c) and η ($|\eta| < 1$) integrated v_2 as a function of collision centrality for Au + Au collisions at $\sqrt{s_{NN}} = 7.7$ GeV (a1), 11.5 GeV (b1), 19.6 GeV (c1), 27 GeV (d1), and 39 GeV (e1). The results in the top panels are presented for several methods of obtaining v_2. The bottom panels show the ratio of v_2 obtained using the various techniques, with respect to $v_2\{2\}$. The error bars shown are statistical.

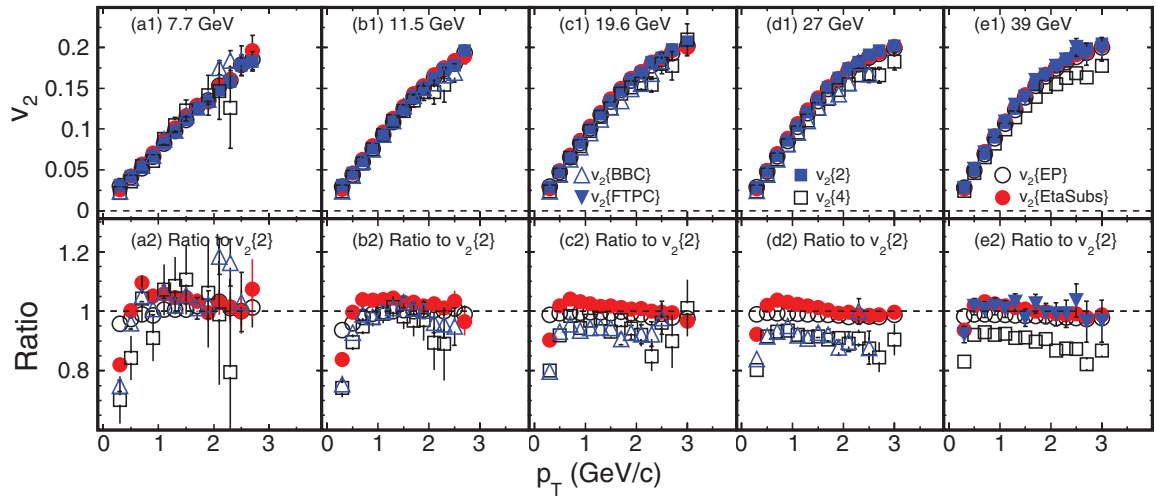

FIG. 5. (Color online) The v_2 as a function of p_T for 20%–30% central Au + Au collisions at midrapidity for $\sqrt{s_{NN}} = 7.7$ GeV (a1), 11.5 GeV (b1), 19.6 GeV (c1), 27 GeV (d1), and 39 GeV (e1). The top panels show v_2 vs p_T using various methods as labeled in the figure and discussed in the text. The bottom panels show the ratio of v_2 measured using the various methods with respect to $v_2\{2\}$.

correlations for peripheral collisions. Nonflow correlations are defined as correlations not related to the reaction plane. The dominant nonflow correlations originating from two-particle correlations (such as HBT correlations, resonance decay) scale as $1/N$ [30], where N is the multiplicity of particles used to determine the event plane. Thus, the nonflow contribution is larger in peripheral collisions. In midcentral and peripheral collisions (10%–20% to 40%–50%), the data of $v_2\{\text{BBC}\}$ from 7.7, 11.5, 19.6, and 27 GeV are consistent with $v_2\{4\}$ and lower than other methods. It suggests that the first-order (BBC) event plane suppresses the second-order nonflow and/or fluctuation effects. Within statistical errors, the results of $v_2\{\text{FTPC}\}$ from Au + Au collisions at $\sqrt{s_{NN}} = 39$ GeV are close to $v_2\{2\}$, $v_2\{\text{EP}\}$, and $v_2\{\text{EtaSubs}\}$ in semicentral collisions (10%–20% to 20%–30%). In the peripheral collisions (30%–40% to 60%–70%), $v_2\{\text{FTPC}\}$ falls between $v_2\{\text{EtaSubs}\}$ and $v_2\{4\}$. It indicates that the η gap between TPC and FTPC reduces the nonflow contribution.

The p_T differential v_2 from various methods for the 20%–30% centrality bin are shown in the upper panels of Fig. 5. For comparison, the v_2 from other methods are divided by the results of the two-particle cumulant method and shown in the lower panels of Fig. 5. It can be seen that the difference of $v_2\{2\}$ compared to $v_2\{\text{FTPC/BBC}\}$, $v_2\{2\}$, and $v_2\{\text{EtaSubs}\}$ depends on the p_T range. A larger difference can be observed in the low-p_T region ($p_T < 1$ GeV/c). Beyond $p_T = 1$ GeV/c the difference stays constant in the measured p_T range. The difference between $v_2\{\text{FTPC/BBC}\}$ and $v_2\{4\}$ is relatively small and less dependent on p_T. It suggests the nonflow contribution to the event plane and two-particle correlation methods depends on p_T. Based on the interpretation in Ref. [1], the difference between $v_2\{2\}^2$ and $v_2\{4\}^2$ is approximately equal to nonflow plus two times v_2 fluctuations. The fact that the ratio of $v_2\{4\}$ to $v_2\{2\}$ is closer to 1 at the lower collision energies indicates that the nonflow and/or v_2 fluctuations in the v_2 measurement depend on the collision energy. One possible explanation is that the nonflow correlations from jets presumably decrease as the collision energy decreases. The results of $v_2\{\text{BBC}\}$ are found to be consistent with $v_2\{4\}$ in 7.7, 11.5, 19.6, and 27 GeV, while the $v_2\{\text{FTPC}\}$ is larger than $v_2\{4\}$ in 39 GeV. This consistency can be also observed in Fig. 4 for 10%–20% to 40%–50% centrality bins. It indicates that the use of the first-order reaction plane (BBC event plane) to study the second harmonic flow eliminates flow fluctuations which are not correlated between different harmonics. The first-order BBC reaction plane is struck by nucleon spectators for these beam energies. The contribution of spectators makes the BBC event plane more sensitive to the reaction plane. This could partly explain the consistency between $v_2\{\text{BBC}\}$ and $v_2\{4\}$ mentioned above. More studies of the collision-energy dependence of nonflow and flow fluctuations will be discussed in another paper.

C. Systematic uncertainties

Different v_2 methods show different sensitivities to nonflow correlations and v_2 fluctuations. In previous STAR publications, the differences between different methods were regarded as systematic uncertainties [11,12]. A great deal of progress has revealed that some of these differences are not attributable to systematic uncertainties in different methods, but attributable to different sensitivities to nonflow and flow fluctuation effects [35,52]. The four-particle cumulant method is less sensitive to nonflow correlations [32,33] and has a negative contribution from flow fluctuations. v_2 measurements from the two-particle cumulant method and the event-plane method (the second harmonic event plane) have positive contributions from flow fluctuations as well as nonflow. It was also noticed that four-particle cumulant results should be very close to flow in the reaction plane, while the two-particle cumulant measures flow in the participant plane [35,52]. Further, because of the large pseudorapidity gap between the BBC/FTPC and TPC, $v_2\{\text{BBC}\}$ and $v_2\{\text{FTPC}\}$ are most insensitive to nonflow correlations.

We estimate the systematic uncertainty on event-plane flattening methods for $v_2\{\mathrm{EP}\}$ and $v_2\{\mathrm{EtaSubs}\}$ by the difference between them and find it to be negligible (below 1%). A 5% systematic uncertainty on $v_2\{\mathrm{BBC}\}$, $v_2\{\mathrm{FTPC}\}$, $v_2\{\mathrm{EP}\}$, and $v_2\{\mathrm{EtaSubs}\}$ is estimated by varying cut parameters (e.g., collision vertex position, the DCA to the primary vertex for the tracks, and the number of fit points used for reconstruction of the tracks). The systematic uncertainties on $v_2\{2\}$ and $v_2\{4\}$ are based on the difference between Q-cumulant and GF-cumulant methods (5%) as well as cut variations (5%). All the percentage uncertainties are relative to the v_2 value.

V. DISCUSSION

A. Transverse momentum and centrality dependence of v_2

The centrality dependence of p_T differential v_2 with respect to the initial eccentricity has been studied in detail for Au + Au and Cu + Cu collisions in $\sqrt{s_{NN}} = 200$ and 62.4 GeV [12,13]. The larger magnitude of v_2 in the more peripheral collisions could be attributable to the larger initial eccentricity in coordinate space for the more peripheral collisions. The participant eccentricity is the initial configuration space eccentricity of the participant nucleons defined by Eq. (3). The root-mean-square participant eccentricity, $\varepsilon_{\mathrm{part}}\{2\}$, is calculated from the MC Glauber model [53,54] (Table II) and color glass condensate (CGC) model [55–58] (Table III). The event plane is constructed from hadrons which have their origin in participant nucleons. At the same time, the event-plane resolution (η subevent) is less than 0.5. Thus, what we actually measure is the root-mean-square of v_2 with respect to the participant plane [52]. In this case, $\varepsilon_{\mathrm{part}}\{2\}$ is the appropriate measure of the initial geometric anisotropy taking the event-by-event fluctuations into account [52,59,60]. In Figs. 6 and 7, the centrality dependence of

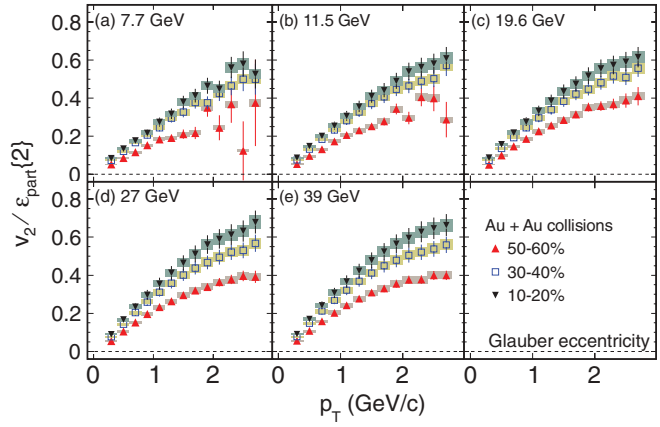

FIG. 6. (Color online) The v_2 over ε (Glauber) as a function of p_T for various collision centralities (10%–20%, 30%–40% and 50%–60%) in Au + Au collisions at midrapidity. Panels (a), (b), (c), (d), and (e) show the results for $\sqrt{s_{NN}} = 7.7$, 11.5, 19.6, 27, and 39 GeV, respectively. The data are from $v_2\{\mathrm{EtaSubs}\}$. The error bars and shaded boxes represent the statistical and systematic uncertainties, respectively, as described in Sec. IV C.

TABLE III. The $\varepsilon_{\mathrm{part}}\{2\}$ and transverse area $\langle S_{\mathrm{part}}\rangle$ from the color glass condensate (CGC) model [55–58] calculations in Au + Au collisions at $\sqrt{s_{NN}} = 7.7$, 11.5, 19.6, 27, 39, 62.4, and 200 GeV. The errors are systematic uncertainties.

Centrality (%)	0–5	5–10	10–20	20–30	30–40	40–50	50–60	60–70	70–80
Au + Au at $\sqrt{s_{NN}} = 7.7$ GeV									
$\varepsilon_{\mathrm{part}}\{2\}$	0.104 ± 0.005	0.19 ± 0.01	0.29 ± 0.01	0.39 ± 0.02	0.47 ± 0.02	0.54 ± 0.03	0.59 ± 0.03	0.62 ± 0.03	0.51 ± 0.02
$\langle S_{\mathrm{part}}\rangle$ (fm^2)	25.9 ± 1.3	21.8 ± 1.1	17.5 ± 0.9	13.4 ± 0.7	10.2 ± 0.5	7.7 ± 0.4	5.5 ± 0.3	3.6 ± 0.2	1.8 ± 0.1
Au + Au at $\sqrt{s_{NN}} = 11.5$ GeV									
$\varepsilon_{\mathrm{part}}\{2\}$	0.104 ± 0.005	0.19 ± 0.01	0.29 ± 0.01	0.39 ± 0.02	0.47 ± 0.02	0.53 ± 0.03	0.59 ± 0.03	0.62 ± 0.03	0.51 ± 0.02
$\langle S_{\mathrm{part}}\rangle$ (fm^2)	25.2 ± 1.2	21.2 ± 1.1	17.0 ± 0.9	13.0 ± 0.7	9.9 ± 0.5	7.5 ± 0.4	5.4 ± 0.3	3.5 ± 0.2	1.8 ± 0.1
Au + Au at $\sqrt{s_{NN}} = 19.6$ GeV									
$\varepsilon_{\mathrm{part}}\{2\}$	0.105 ± 0.005	0.19 ± 0.01	0.29 ± 0.01	0.39 ± 0.02	0.47 ± 0.02	0.53 ± 0.03	0.58 ± 0.03	0.61 ± 0.03	0.51 ± 0.02
$\langle S_{\mathrm{part}}\rangle$ (fm^2)	24.4 ± 1.2	20.6 ± 1.0	16.6 ± 0.9	12.6 ± 0.7	9.7 ± 0.5	7.3 ± 0.4	5.3 ± 0.3	3.5 ± 0.2	1.8 ± 0.1
Au + Au at $\sqrt{s_{NN}} = 27$ GeV									
$\varepsilon_{\mathrm{part}}\{2\}$	0.105 ± 0.005	0.19 ± 0.01	0.29 ± 0.01	0.39 ± 0.02	0.47 ± 0.02	0.53 ± 0.03	0.58 ± 0.03	0.61 ± 0.03	0.51 ± 0.02
$\langle S_{\mathrm{part}}\rangle$ (fm^2)	24.1 ± 1.2	20.3 ± 1.0	16.4 ± 0.8	12.5 ± 0.6	9.6 ± 0.5	7.2 ± 0.4	5.3 ± 0.3	3.5 ± 0.2	1.8 ± 0.1
Au + Au at $\sqrt{s_{NN}} = 39$ GeV									
$\varepsilon_{\mathrm{part}}\{2\}$	0.105 ± 0.005	0.19 ± 0.01	0.29 ± 0.01	0.39 ± 0.02	0.47 ± 0.02	0.53 ± 0.03	0.58 ± 0.03	0.61 ± 0.03	0.50 ± 0.02
$\langle S_{\mathrm{part}}\rangle$ (fm^2)	23.9 ± 1.2	20.1 ± 1.0	16.2 ± 0.8	12.4 ± 0.6	9.5 ± 0.5	7.2 ± 0.4	5.3 ± 0.3	3.5 ± 0.2	1.8 ± 0.1
Au + Au at $\sqrt{s_{NN}} = 62.4$ GeV									
$\varepsilon_{\mathrm{part}}\{2\}$	0.105 ± 0.005	0.19 ± 0.01	0.29 ± 0.01	0.39 ± 0.02	0.47 ± 0.02	0.53 ± 0.03	0.58 ± 0.03	0.61 ± 0.03	0.50 ± 0.02
$\langle S_{\mathrm{part}}\rangle$ (fm^2)	23.7 ± 1.2	20.0 ± 1.0	16.1 ± 0.8	12.3 ± 0.6	9.4 ± 0.5	7.2 ± 0.4	5.3 ± 0.3	3.5 ± 0.2	1.8 ± 0.1
Au + Au at $\sqrt{s_{NN}} = 200$ GeV									
$\varepsilon_{\mathrm{part}}\{2\}$	0.104 ± 0.005	0.19 ± 0.01	0.29 ± 0.01	0.39 ± 0.02	0.47 ± 0.02	0.53 ± 0.03	0.57 ± 0.03	0.60 ± 0.03	0.49 ± 0.02
$\langle S_{\mathrm{part}}\rangle$ (fm^2)	23.7 ± 1.2	20.0 ± 1.0	16.1 ± 0.8	12.3 ± 0.6	9.4 ± 0.5	7.2 ± 0.4	5.3 ± 0.3	3.6 ± 0.2	1.9 ± 0.1

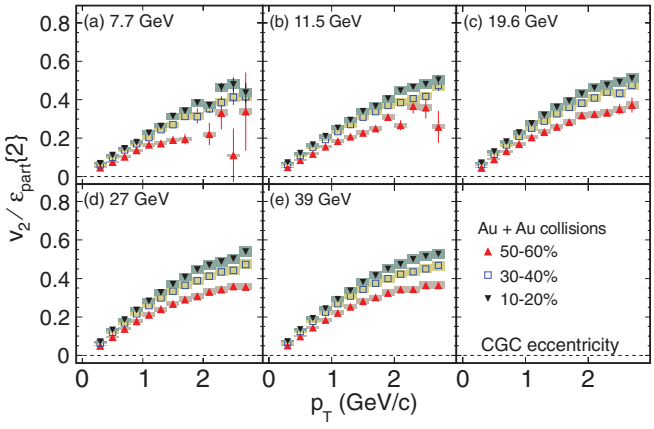

FIG. 7. (Color online) The v_2 over ε (CGC) as a function of p_T for various collision centralities (10%–20%, 30%–40%, and 50%–60%) in Au + Au collisions at midrapidity. Panels (a), (b), (c), (d), and (e) show the results for $\sqrt{s_{NN}} = 7.7$, 11.5, 19.6, 27, and 39 GeV, respectively. The data are from $v_2\{\text{EtaSubs}\}$. The error bars and shaded boxes represent the statistical and systematic uncertainties respectively, as described in Sec. IV C.

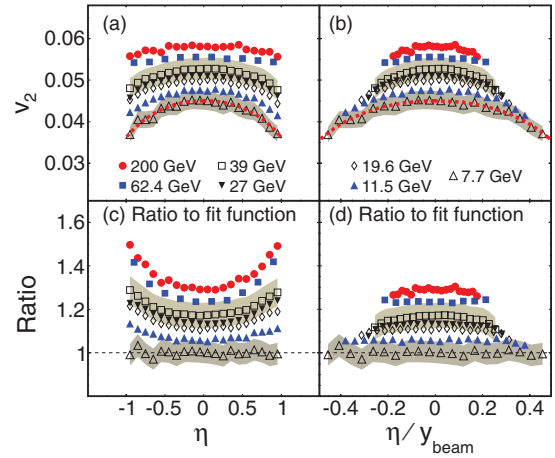

FIG. 8. (Color online) Panel (a) shows the $v_2\{\text{EP}\}$ vs η for 10%–40% centrality in Au + Au collisions at $\sqrt{s_{NN}} = 7.7$, 11.5, 19.6, 27, 39, 62.4, and 200 GeV. Panel (c) shows the ratio of v_2 vs η for all $\sqrt{s_{NN}}$ with respect to the fit curve. Panel (b) shows the $v_2\{\text{EP}\}$ vs η/y_{beam}. Panel (d) shows the ratio of v_2 vs η/y_{beam} for all $\sqrt{s_{NN}}$ with respect to the fit curve. The data for $\sqrt{s_{NN}} = 62.4$ and 200 GeV are from Refs. [12,61,62]. The dashed red curves show the empirical fit to the results from Au + Au collisions at $\sqrt{s_{NN}} = 7.7$ GeV. The bands show the systematic uncertainties as described in Sec. IV C.

p_T differential v_2 over eccentricity is shown for Au + Au collisions at $\sqrt{s_{NN}} = 7.7$, 11.5, 19.6, 27, and 39 GeV. For all five collision energies, the centrality dependence of $v_2(p_T)$ is observed to be similar to that at higher collision energies (62.4 and 200 GeV) of Au + Au and Cu + Cu colliding systems. That central collisions in general have higher v_2/ε than peripheral collisions is consistent with the picture that collective interactions are stronger in collisions with larger numbers of participants.

B. Pseudorapidity dependence

The panel (a) of Fig. 8 shows v_2 as a function of pseudorapidity for Au + Au collisions at $\sqrt{s_{NN}} = 7.7$, 11.5, 19.6, 27, 39, 62.4, and 200 GeV in midcentral (10%–40%) collisions. The data for $\sqrt{s_{NN}} = 62.4$ and 200 GeV are from Refs. [12,61,62]. To facilitate comparison with 62.4 and 200 GeV data, the results of $v_2\{\text{EP}\}$ are selected for the rest of the collision energies. The 7.7-GeV data are empirically fit by the following function:

$$v_2(\eta) = p_0 + p_1\eta^2 + p_2\eta^4, \tag{45}$$

with parameters $p_0 = 0.0450 \pm 0.0002$, $p_1 = -0.0064 \pm 0.0015$, $p_2 = -0.0024 \pm 0.0017$. For clarity, panel (c) of Fig. 8 shows the ratio of $v_2(\eta)$ with respect to this fit function. The pseudorapidity dependence of v_2 indicates a change in shape as we move from $\sqrt{s_{NN}} = 200$ GeV to 7.7 GeV within our measured range $-1 < \eta < 1$.

To investigate the collision energy dependence of the $v_2(\eta)$ shape, in panels (b) and (d) of Fig. 8, the same v_2 results have been plotted as a function of pseudorapidity divided by beam rapidity. The data of 7.7 GeV are fit by Eq. (45) with parameters $p_0 = 0.0450 \pm 0.0002$, $p_1 = -0.0279 \pm 0.0064$, and $p_2 = -0.0464 \pm 0.0325$. The beam rapidities are 2.09, 2.50, 3.04, 3.36, 3.73, 4.20, and 5.36 for $\sqrt{s_{NN}} = 7.7$, 11.5, 19.6, 27, 39, 62.4, and 200 GeV, respectively. After dividing pseudorapidity by the beam rapidity, the shape of v_2 seems similar at all collision energies. The approximate beam rapidity scaling on the $v_2(\eta)$ shape suggests the change in shape may be related to the final particle density. Higher particle density indicates higher probability of interaction, which can generate larger collective flow.

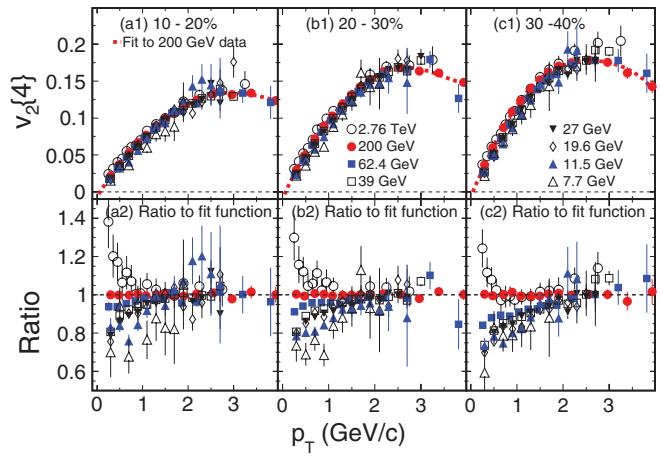

FIG. 9. (Color online) The top panels show $v_2\{4\}$ vs p_T at midrapidity for various collision energies ($\sqrt{s_{NN}} = 7.7$ GeV to 2.76 TeV). The results for $\sqrt{s_{NN}} = 7.7$ to 200 GeV are for Au + Au collisions and those for 2.76 TeV are for Pb + Pb collisions. The dashed red curves show the empirical fits to the results from Au + Au collisions at $\sqrt{s_{NN}} = 200$ GeV. The bottom panels show the ratio of $v_2\{4\}$ vs p_T for all $\sqrt{s_{NN}}$ with respect to the fit curve. The results are shown for three collision centrality classes: 10%–20% (a1), 20%–30% (b1), and 30%–40% (c1). Error bars are shown only for the statistical uncertainties.

TABLE IV. Summary of the parameters for the fit functions to the results of $v_2\{4\}$ vs p_T in Au + Au collisions at $\sqrt{s_{NN}} = 200$ GeV.

Parameters	p_0	p_1	p_2	p_3	p_4	p_5
10%–20%	-0.00730 ± 0.00114	0.10785 ± 0.00598	-0.03941 ± 0.01038	0.01508 ± 0.00767	-0.00411 ± 0.00246	0.00041 ± 0.00028
20%–30%	-0.00890 ± 0.00096	0.14250 ± 0.00500	-0.05206 ± 0.00869	0.02156 ± 0.00642	-0.00685 ± 0.00206	0.00077 ± 0.00023
30%–40%	-0.00581 ± 0.00206	0.14526 ± 0.01089	-0.00529 ± 0.01910	-0.02409 ± 0.01419	0.00797 ± 0.00456	-0.00084 ± 0.00052

C. Energy dependence

One of the most important experimental observations at RHIC is the significant v_2 signal in the top energy of Au + Au collisions [6,10] (more than 50% larger than at the SPS [63]). It could be interpreted as the observation of a higher degree of thermalization than at lower collision energies [6]. The BES data from the RHIC-STAR experiment offers an opportunity to study the collision energy dependence of v_2 using a wide acceptance detector at midrapidity. Figure 9 shows the p_T dependence of $v_2\{4\}$ from $\sqrt{s_{NN}} = 7.7$ GeV to 2.76 TeV in 10%–20% (a1), 20%–30% (b1), and 30%–40% (c1) centrality bins, where the ALICE results in Pb + Pb collisions at $\sqrt{s_{NN}} = 2.76$ TeV are taken from Ref. [18]. The reasons to select the results of $v_2\{4\}$ for the comparison are the following: (1) to keep the method for v_2 measurements consistent with the published results of ALICE; (2) because $v_2\{4\}$ is insensitive to nonflow correlations. The 200-GeV data are empirically fit by a fifth-order polynomial function. The parameters for the fit function are listed in Table IV. For comparison, the v_2 from other energies are divided by the fit and shown in the lower panels of Fig. 9. We choose 200-GeV data as the reference because the statistical errors are smallest. For p_T below 2 GeV/c, the v_2 values rise with increasing collision energy. Beyond $p_T = 2$ GeV/c the v_2 results show comparable values within statistical errors.

The increase of $v_2(p_T)$ as a function of energy could be attributable to the change of chemical composition from low to high energies [22] and/or larger collectivity at the higher collision energy. The baryonic chemical potential varies a lot (20–400 MeV) from 200 to 7.7 GeV [22]. The baryon over meson ratio is larger in lower collisions energies. The difference of v_2 for baryon and meson, for example, proton v_2 < pion v_2 for p_T below 2 GeV/c, could partly explain the collision energy dependence. Further, in Fig. 10 we compare the experimental data from Fig. 9 (b2) to the viscous hydrodynamic calculations [5]. As the collision energy varies from $\sqrt{s_{NN}} = 7.7$ to 2760 GeV, the experimental data show larger splitting in the lower p_T region and converge at the intermediate range ($p_T \sim 2$ GeV/c), while, in the pure viscous hydrodynamic simulations, the splitting increases with p_T. The p_T dependence of the v_2 ratio cannot be reproduced by pure viscous hydrodynamic simulations with a constant shear viscosity to entropy density ratio (η/s) and zero net baryon density. The comparison suggests that a quantitative study at lower collision energies requires a more serious theoretical approach, such as three-dimensional viscous hydro + UrQMD with a consistent EOS at nonzero baryon chemical potential.

Figure 11 shows the energy dependence of $v_2\{\text{EtaSubs}\}$. Larger $v_2\{\text{EtaSubs}\}$ values are observed at higher collision energy for a selected p_T bin, but the p_T dependence of the difference is quite different from $v_2\{4\}$. The ratios to 39-GeV data for each collision energy first decrease as a function of p_T, then slightly increase in the p_T region of 1–2.5 GeV/c. The different trend of the energy dependence of v_2 from $v_2\{4\}$ and $v_2\{\text{EtaSubs}\}$ is interpreted as owing to the different sensitivity of the v_2 methods to nonflow and/or flow fluctuations.

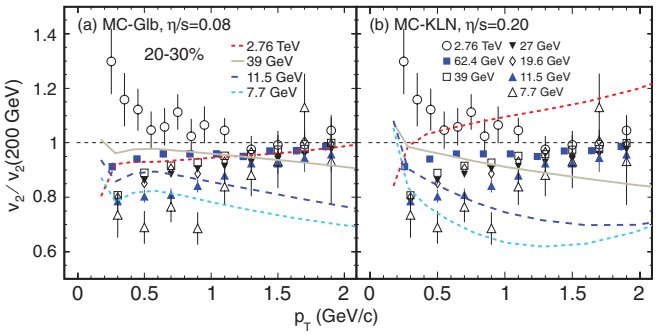

FIG. 10. (Color online) The experimental data (symbols) are the same as in Fig. 9 (b2). The lines represent the viscous hydrodynamic calculations from Ref. [5] based on (a) MC-Glauber initial conditions and $\eta/s = 0.08$ and (b) MC-KLN initial conditions and $\eta/s = 0.20$.

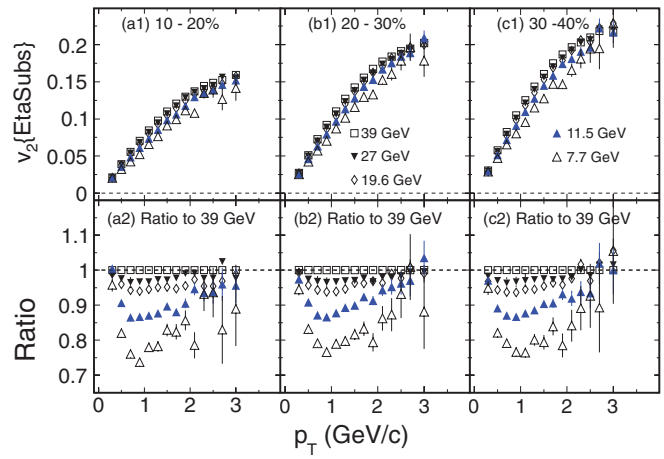

FIG. 11. (Color online) The top panels show $v_2\{\text{EtaSubs}\}$ vs p_T at midrapidity for various collision energies ($\sqrt{s_{NN}} = 7.7$ GeV to 39 GeV). The bottom panels show the ratio of $v_2\{\text{EtaSubs}\}$ vs p_T for all $\sqrt{s_{NN}}$ with respect to the 39-GeV data. The results are shown for three collision centrality classes: 10%–20% (a1), 20%–30% (b1), and 30%–40% (c1). Error bars are shown only for the statistical uncertainties.

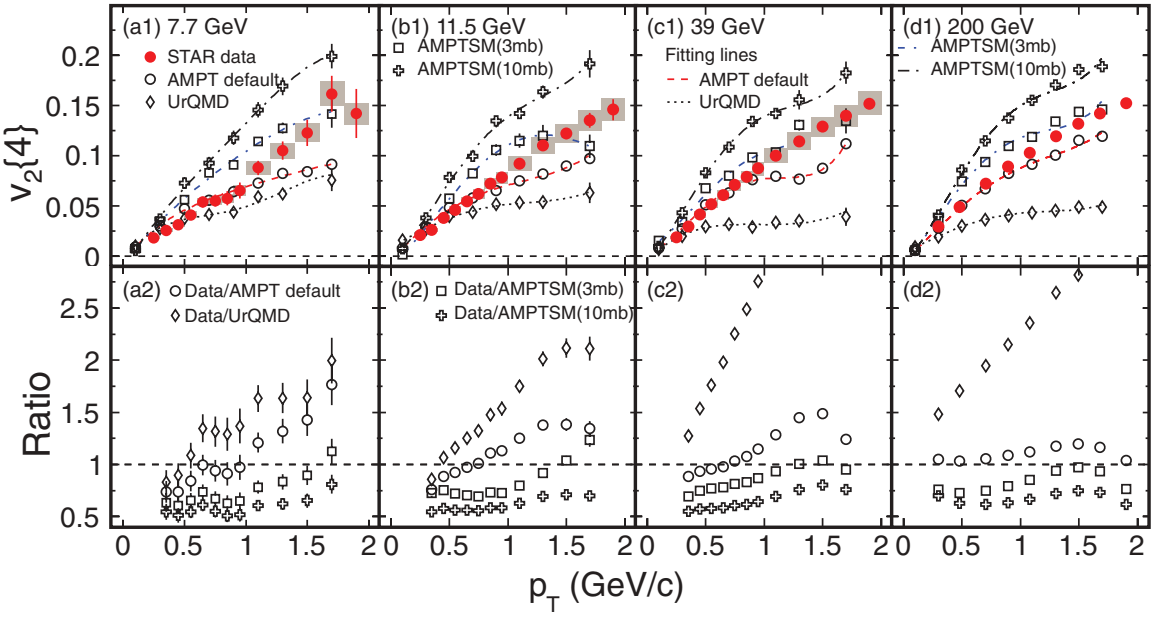

FIG. 12. (Color online) The $v_2\{4\}$ as a function of p_T for 20%–30% Au + Au collisions at $\sqrt{s_{NN}} = 7.7$, 11.5, 39, and 200 GeV compared to corresponding results from UrQMD, AMPT default version, and AMPT with string melting version (3 and 10 mb). The shaded boxes show the systematic uncertainties for the experimental data of 7.7, 11.5, and 39 GeV. The bottom panels show the ratio of data to the fit results of the models.

D. Model comparisons

To investigate the partonic and hadronic contribution to the final v_2 results from different collision energies, transport model calculations from AMPT default (version 1.11), AMPT string melting (version 2.11) [64], and UrQMD (version 2.3) [65] are compared with the new data presented. The initial parameter settings for the models follow the recommendation in the cited references. The AMPT default and UrQMD models only take the hadronic interactions into consideration, while the AMPT string-melting version incorporates both partonic and hadronic interactions. The larger the parton cross section, the later the hadron cascade starts.

Figure 12 shows the comparison of p_T differential $v_2\{4\}$ between model and data in the 20%–30% centrality bin. The 200-GeV data are taken from Ref. [62]. The figure shows that UrQMD underpredicts the measurements at $\sqrt{s_{NN}} = 39$ and 200 GeV in the p_T range studied. The differences are reduced as the collision energy decreases. That the ratio of data to UrQMD results are closer to 1 at the lower collision energy indicates that the contribution of hadronic interactions becomes more significant at lower collision energies. The AMPT model with default settings underpredicts the 200-GeV data, while the ratios of data to AMPT default results show no significant change from 7.7 to 39 GeV. The inconsistency between AMPT default and UrQMD makes the conclusion model dependent. The AMPT model with string-melting version with 3- and 10-mb parton cross sections overpredicts the results at all collision energies from 7.7 to 200 GeV. A larger parton cross section means stronger partonic interactions which translate into a larger magnitude of v_2. The difference between data and these AMPT model calculations seems to show no significantly systematic change vs collision energies. However, a recent study with the AMPT model suggests hadronic potentials affect the final v_2 results significantly when the collision energy is less than $\sqrt{s_{NN}} = 39$ GeV [66].

VI. SUMMARY

We have presented elliptic flow, v_2, measurements from Au + Au collisions at $\sqrt{s_{NN}} = 7.7$, 11.5, 19.6, 27, and 39 GeV for inclusive charged hadrons at midrapidity. To investigate nonflow correlations and v_2 fluctuations, various measurement methods have been used in the analysis. The difference between $v_2\{2\}$ and $v_2\{4\}$ decreases with decrease in collision energy, indicating that nonflow contribution and/or flow fluctuations decrease with a decrease in collision energy. The centrality and p_T dependence of v_2 are similar to that observed at higher RHIC collision energies. A larger v_2 is observed in more peripheral collisions. The pseudorapidity dependence of v_2 indicates a change in shape from 200 to 7.7 GeV within the measured range $-1 < \eta < 1$, but the results of v_2 versus pseudorapidity scaled by beam rapidity shows a similar trend for all collision energies. The comparison with Au + Au collisions at higher energies at RHIC ($\sqrt{s_{NN}} =$ 62.4 and 200 GeV) and at LHC (Pb + Pb collisions at $\sqrt{s_{NN}} =$ 2.76 TeV) shows the $v_2\{4\}$ values at low p_T ($p_T < 2.0\,\mathrm{GeV}/c$) increase with increase in collision energy implying an increase of collectivity. The current viscous hydrodynamic simulations cannot reproduce the trend of the energy dependence of $v_2(p_T)$.

The agreement between the data and UrQMD, which is based on hadronic rescatterings, improves at lower collision energies, consistent with an increasing role of the hadronic stage at these energies. The inconsistency between AMPT default and UrQMD makes the conclusion model dependent. The comparison to AMPT model calculations seems to show no significantly systematic change vs collision energy, but im-

proved calculations including harmonic potentials may change the v_2 values from AMPT models at lower collision energies.

These results set the baseline to study the number of constituent quark scaling of identified hadron v_2. It also sets the stage for understanding the collision energy dependence of v_2 in the regime where the relative contribution of baryon and mesons vary significantly.

ACKNOWLEDGMENTS

We thank the RHIC Operations Group and RCF at BNL, the NERSC Center at LBNL, and the Open Science Grid consortium for providing resources and support. This work was supported in part by the Offices of NP and HEP within the US DOE Office of Science, the US NSF, the Sloan Foundation; CNRS/IN2P3; FAPESP CNPq of Brazil; Ministry of Education and Science of the Russian Federation; NNSFC, CAS, MoST, and MoE of China; GA and MSMT of the Czech Republic; FOM and NWO of the Netherlands; DAE, DST, and CSIR of India; Polish Ministry of Science and Higher Education; Korea Research Foundation; Ministry of Science, Education, and Sports of the Republic of Croatia; and RosAtom of Russia.

[1] S. A. Voloshin, A. M. Poskanzer, and R. Snellings, in *Landolt-Boernstein, Relativistic Heavy Ion Physics*, Vol. 1/23 (Springer-Verlag, Berlin, 2010), pp. 5–54.
[2] P. Sorensen, arXiv:0905.0174.
[3] R. Snellings, New J. Phys. **13**, 055008 (2011).
[4] J. Y. Ollitrault, Phys. Rev. D **46**, 229 (1992).
[5] C. Shen and U. Heinz, Phys. Rev. C **85**, 054902 (2012).
[6] K. H. Ackermann *et al.* (STAR Collaboration), Phys. Rev. Lett. **86**, 402 (2001).
[7] J. Adams *et al.* (STAR Collaboration), Phys. Rev. Lett. **92**, 052302 (2004).
[8] J. Adams *et al.* (STAR Collaboration), Phys. Rev. Lett. **95**, 122301 (2005).
[9] J. Adams *et al.* (STAR Collaboration), Nucl. Phys. A **757**, 102 (2005).
[10] J. Adams *et al.* (STAR Collaboration), Phys. Rev. C **72**, 014904 (2005).
[11] B. I. Abelev *et al.* (STAR Collaboration), Phys. Rev. Lett. **99**, 112301 (2007).
[12] B. I. Abelev *et al.* (STAR Collaboration), Phys. Rev. C **77**, 054901 (2008).
[13] B. I. Abelev *et al.* (STAR Collaboration), Phys. Rev. C **81**, 044902 (2010).
[14] S. S. Adler *et al.* (PHENIX Collaboration), Phys. Rev. Lett. **91**, 182301 (2003).
[15] S. S. Adler *et al.* (PHENIX Collaboration), Phys. Rev. Lett. **94**, 232302 (2005).
[16] B. Alver *et al.* (PHOBOS Collaboration), Phys. Rev. Lett. **98**, 242302 (2007).
[17] H. Appelshauser *et al.* (NA49 Collaboration), Phys. Rev. Lett. **80**, 4136 (1998).
[18] K. Aamodt *et al.* (ALICE Collaboration), Phys. Rev. Lett. **105**, 252302 (2010).
[19] G. Aad *et al.* (ATLAS Collaboration), Phys. Lett. B **707**, 330 (2012).
[20] B. Mohanty (STAR Collaboration), J. Phys. G **38**, 124023 (2011).
[21] J. Cleymans, H. Oeschler, K. Redlich, and S. Wheaton, Phys. Rev. C **73**, 034905 (2006); F. Becattini, J. Manninen, and M. Gazdzicki, *ibid.* **73**, 044905 (2006); A. Andronic, P. Braun-Munzinger, and J. Stachel, Nucl. Phys. A **772**, 167 (2006).
[22] L. Kumar (STAR Collaboration), J. Phys. G **38**, 124145 (2011).
[23] J. Cleymans, H. Oeschler, K. Redlich, and S. Wheaton, Phys. Rev. C **73**, 034905 (2006).
[24] Y. Aoki *et al.*, Nature (London) **443**, 675 (2006).
[25] S. Ejiri, Phys. Rev. D **78**, 074507 (2008).
[26] M. A. Stephanov, Int. J. Mod. Phys. A **20**, 4387 (2005).
[27] B. Mohanty, Nucl. Phys. A **830**, 899c (2009), and references therein.
[28] P. F. Kolb, J. Sollfrank, and U. Heinz, Phys. Rev. C **62**, 054909 (2000).
[29] H. Sorge, Phys. Rev. Lett. **82**, 2048 (1999).
[30] A. M. Poskanzer and S. A. Voloshin, Phys. Rev. C **58**, 1671 (1998).
[31] S. Wang *et al.*, Phys. Rev. C **44**, 1091 (1991).
[32] N. Borghini, P. M. Dinh, and J.-Y. Ollitrault, Phys. Rev. C **63**, 054906 (2001).
[33] N. Borghini, P. M. Dinh, and J.-Y. Ollitrault, Phys. Rev. C **64**, 054901 (2001).
[34] R. S. Bhalerao, N. Borghini, and J. Y. Ollitrault, Nucl. Phys. A **727**, 373 (2003).
[35] S. A. Voloshin, A. M. Poskanzer, A. Tang, and G. Wang, Phys. Lett. B **659**, 537 (2008).
[36] Md. Nasim, L. Kumar, P. K. Netrakanti, and B. Mohanty, Phys. Rev. C **82**, 054908 (2010).
[37] C. A. Whitten, Jr. (STAR Collaboration), AIP Conf. Proc. **980**, 390 (2008).
[38] C. Adler *et al.* (STAR Collaboration), Nucl. Instrum. Methods A **470**, 488 (2001).
[39] W. J. Llope *et al.* (STAR Collaboration), Nucl. Instrum. Methods A **522**, 252 (2004).
[40] B. Bonner *et al.* (STAR Collaboration), Nucl. Instrum. Methods A **508**, 181 (2003); M. Shao *et al.* (STAR Collaboration), *ibid.* **558**, 419 (2006).
[41] K. H. Ackermann *et al.* (STAR Collaboration), Nucl. Instrum. Methods A **499**, 624 (2003).
[42] K. H. Ackermann *et al.* (STAR Collaboration), Nucl. Instrum. Methods A **499**, 713 (2003).
[43] B. I. Abelev *et al.* (STAR Collaboration), Phys. Rev. C **81**, 024911 (2010).
[44] D. Kharzeev and M. Nardi, Phys. Lett. B **507**, 121 (2001).
[45] K. Nakamura *et al.* (Particle Data Group), J. Phys. G **37**, 075021 (2010).
[46] B. B. Back *et al.* (PHOBOS Collaboration), Phys. Rev. C **70**, 021902(R) (2004).
[47] J. Barrette *et al.* (E877 Collaboration), Phys. Rev. C **55**, 1420 (1997); I. Selyuzhenkov and S. Voloshin, *ibid.* **77**, 034904 (2008).
[48] J. Barrette *et al.* (E877 Collaboration), Phys. Rev. C **56**, 3254 (1997).
[49] G. Agakishiev *et al.* (STAR Collaboration), Phys. Rev. C **85**, 014901 (2012).

[50] A. Bilandzic, R. Snellings, and S. Voloshin, Phys. Rev. C **83**, 044913 (2011).
[51] A. Bilandzic, Ph.D. thesis, Nikhef and Utrecht University, 2011.
[52] J. Y. Ollitrault, A. M. Poskanzer, and S. A. Voloshin, Phys. Rev. C **80**, 014904 (2009).
[53] M. Miller and R. Snellings, arXiv:nucl-ex/0312008.
[54] M. L. Miller, K. Reygers, S. J. Sanders, and P. Steinberg, Annu. Rev. Nucl. Part. Sci. **57**, 205 (2007).
[55] A. Adil, H. J. Drescher, A. Dumitru, A. Hayashigaki, and Y. Nara, Phys. Rev. C **74**, 044905 (2006).
[56] H. J. Drescher and Y. Nara, Phys. Rev. C **75**, 034905 (2007).
[57] H. J. Drescher and Y. Nara, Phys. Rev. C **76**, 041903 (2007).
[58] T. Hirano and Y. Nara, Phys. Rev. C **79**, 064904 (2009).
[59] S. Voloshin, arXiv:nucl-th/0606022.
[60] B. Alver *et al.* (PHOBOS Collaboration), Phys. Rev. C **77**, 014906 (2008).
[61] B. I. Abelev *et al.* (STAR Collaboration), Phys. Rev. C **75**, 054906 (2007).
[62] Y. Bai, Ph.D. thesis, Nikhef and Utrecht University, 2007.
[63] A. M. Poskanzer and S. A. Voloshin (NA49 Collaboration), Nucl. Phys. A **661**, 341c (1999).
[64] Z. W. Lin, C. M. Ko, B. A. Li, B. Zhang, and S. Pal, Phys. Rev. C **72**, 064901 (2005).
[65] H. Petersen *et al.*, arXiv:0805.0567.
[66] J. Xu, L. W. Chen, C. M. Ko, and Z. W. Lin, Phys. Rev. C **85**, 041901 (2012).